Energy & Environmental Science

Quantitative Relationships between Film Morphology, Charge Carrier Dynamics, and Photovoltaic Performance in Bulk-Heterojunction Binary vs Ternary Acceptor Blends

Journal:	*Energy & Environmental Science*
Manuscript ID	EE-ART-12-2022-003883.R1
Article Type:	Paper
Date Submitted by the Author:	25-Jan-2023

Complete List of Authors:	Zhu, Weigang; Tianjin University, Department of Chemistry Li, Guoping; Northwestern University, Chemistry; Mukherjee, Subhrangsu; National Institute of Standards and Technology Material Measurement Laboratory Powers-Riggs, Natalia; SLAC, PULSE Institute; SLAC Jones, Leighton; Northwestern University, Chemistry Gann, Eliot; National Institute of Standards and Technology, Material Measurement Lab Kline, R. Joseph; National Institute of Standards and Technology, Material Measurement Laboratory Herzing, Andrew; National Institute of Standards and Technology, SMSD Logsdon, Jenna; Northwestern University, Department of Chemistry Flagg, Lucas; National Institute of Standards and Technology Materials Science and Engineering Laboratory Stern, Charlotte; Northwestern University, Chemistry Young, Ryan; Northwestern University, Department of Chemistry Kohlstedt, Kevin; Northwestern University, Chemistry Schatz, George; Northwestern University, Chemistry Delongchamp, Dean; National Institute of Standards and Technology, Polymers Wasielewski, Michael; Northwestern University, Department of Chemistry Melkonyan, Ferdinand ; Northwestern University, Chemistry Facchetti, Antonio; Northwestern University, Department of Chemistry and the Materials Research Center Marks, Tobin; Northwestern University, Chemistry

Broader context

Bulk-heterojunction (BHJ) polymer solar cells (PSCs) offer the attractions of earth-abundant starting materials, structure and properties tunability via "green" chemical reactions, large-area solution processability, light weight, minimal toxicity, and mechanical flexibility, which together make it ideal as one of the promising next generation solar energy harvesting technologies. Nevertheless, current leading research directions in the field remain focused on the fundamental mechanistic studies, and a clear relationship between BHJ morphology structure, photophysics, and device performance is still lacking in polymer-nonfullerene binary and polymer-nonfullerene-fullerene ternary systems. Here we systematically investigate BHJ blends of the **PBDB-TF** donor polymer, indacenodithienothiophene-based non-fullerene (NFA) material **ITIC-Th**, Y6-based NFA material **BTBOL4F**, and fullerene **$PC_{71}BM$**, using nanostructural, crystallographic, morphological, transient absorption spectroscopy, Density Functional Theory, single carrier diodes, and inverted solar cell analysis probes. The results reveal that incorporation of **$PC_{71}BM$** into **ITIC-Th** binary system changes molecular orientation, crystallinity, domain size, and BHJ upper surface composition, therefore change electron delocalization, charge mobility, bimolecular recombination, and thus solar cell J_{SC}, FF, PCE metrics. Single crystal X-ray diffraction and DFT calculations reveal the intricate structural relationships of molecular packing and electronic properties such as reorganization energy, electronic coupling, charge delocalization, and excited-state energetics. Overall, this contribution provides general quantitative morphology-charge dynamics-device performance design rules for future PSC development.

Quantitative Relationships between Film Morphology, Charge Carrier Dynamics, and Photovoltaic Performance in Bulk-Heterojunction Binary vs Ternary Acceptor Blends

Weigang Zhu[†,1,4], Guoping Li[†,1], Subhrangsu Mukherjee[2], Natalia E. Powers-Riggs[1], Leighton O. Jones[1], Eliot Gann[2], R. Joseph Kline[2], Andrew Herzing[2], Jenna L. Logsdon[1], Lucas Flagg[2], Charlotte L. Stern[1], Ryan M. Young[1], Kevin L. Kohlstedt[1]*, George C. Schatz[1]*, Dean M. DeLongchamp[2]*, Michael R. Wasielewski[1]*, Ferdinand S. Melkonyan[1]*, Antonio Facchetti[1,3]*, Tobin J. Marks[1]*

[1]Department of Chemistry, and the Materials Research Center, Northwestern University, 2145 Sheridan Road, Evanston, Illinois, 60208, United States

[2]Material Measurement Laboratory, National Institute of Standards and Technology, Gaithersburg, Maryland 20899, United States

[3]Flexterra Corporation, 8025 Lamon Avenue, Skokie, Illinois 60077, United States

[4]Tianjin Key Laboratory of Molecular Optoelectronic Sciences, Department of Chemistry, School of Science, Tianjin University, Tianjin 300072, China

[†]These two authors contributed equally to this work

*E-mail: kkohlstedt@northwestern.edu (K.L.K.); g-schatz@northwestern.edu (G.C.S.); dean.delongchamp@nist.gov (D.M.D.); m-wasielewski@northwestern.edu (M.R.W.); fmelkonyan@gmail.com (F.S.M.); a-facchetti@northwestern.edu (A.F.); t-marks@northwestern.edu (T.J.M.)

ORCID ID:
Weigang Zhu, 0000-0002-5888-4481
Guoping Li, 0000-0002-8193-9639
Subhrangsu Mukherjee, 0000-0002-5479-3750
Natalia E. Powers-Riggs, 0000-0002-9309-9622
Leighton O. Jones, 0000-0001-6657-2632
Eliot Gann, 0000-0001-5570-8880
R. Joseph Kline, 0000-0003-4693-9083
Andrew Herzing, 0000-0001-5944-2610
Jenna L. Logsdon, 0000-0003-2000-3770
Lucas Flagg, 0000-0002-2798-5650
Charlotte L. Stern, 0000-0002-9491-289X
Ryan M. Young, 0000-0002-5108-0261
Kevin L. Kohlstedt, 0000-0001-8045-0930
George C. Schatz, 0000-0001-5837-4740
Dean M. DeLongchamp, 0000-0003-0840-0757
Michael R. Wasielewski, 0000-0003-2920-5440
Ferdinand S. Melkonyan, 0000-0001-8228-9247
Antonio Facchetti, 0000-0002-8175-7958
Tobin J. Marks, 0000-0001-8771-0141

Broader context

Bulk-heterojunction (BHJ) polymer solar cells (PSCs) offer the attractions of earth-abundant starting materials, structure and properties tunability via "green" chemical reactions, large-area solution processability, light weight, minimal toxicity, and mechanical flexibility, which together make them ideal as one of the promising next-generation solar energy harvesting technologies. Nevertheless, current leading research directions in the field remain focused on the fundamental mechanistic studies, and a clear relationship between BHJ morphology structure, photophysics, and device performance is still lacking in polymer-nonfullerene binary and polymer-nonfullerene-fullerene ternary systems. Here we systematically investigate BHJ blends of the **PBDB-TF** donor polymer, indacenodithienothiophene-based non-fullerene (NFA) material **ITIC-Th**, Y6-based NFA material **BTBOL4F**, and fullerene **$PC_{71}BM$**, using nanostructural crystallographic, morphological, transient absorption spectroscopy, Density Functional Theory, single carrier diodes, and inverted solar cell analysis probes. The results reveal that incorporation of **$PC_{71}BM$** into **ITIC-Th** binary system changes molecular orientation, crystallinity, domain size, and BHJ upper surface composition, and therefore change electron delocalization, charge mobility, bimolecular recombination, and thus solar cell J_{SC}, FF, and PCE metrics. Single crystal X-ray diffraction and DFT calculations reveal the intricate structural relationships of molecular packing and electronic properties such as reorganization energy, electronic coupling, charge delocalization, and excited-state energetics. Overall, this contribution provides general quantitative morphology-charge dynamics-device performance design rules for future PSC development.

Abstract

Addressing pertinent and perplexing questions regarding why nonfullerene acceptors (NFAs) promote higher power conversion efficiencies (PCEs) than traditional fullerenes and how photoactive bulk heterojunction (BHJ) film morphology, charge photogeneration, and recombination dynamics dictate solar cell performance have stimulated many studies of polymer solar cells (PSCs), yet quantitative relationships remain limited. Better understanding in these areas offers the potential to advance materials design and device engineering, afford higher PCEs, and ultimate commercialization. Here we probe quantitative relationships between BHJ film morphology, charge carrier dynamics, and photovoltaic performance in model binary and ternary blend systems having a wide bandgap donor polymer, a fullerene, and a promising NFA. We show that optimal **$PC_{71}BM$** incorporation in a **PBDB-TF:ITIC-Th** binary system matrix retains the original π-face-on orientation, **ITIC-Th** crystallinity and BHJ film crystallite dimensions, and reduces film upper surface **ITIC-Th** segregation. Such morphology changes together simultaneously increase hole (μ_h) and electron (μ_e) mobilities, facilitate light-activated **ITIC-Th** to **$PC_{71}BM$** domain electron delocalization, reduce free charge carrier (FC) bimolecular recombination (BR) within **PBDB-TF:ITIC-Th** mixed regions, and increase FC extraction pathways via **PBDB-TF:$PC_{71}BM$** pairs. The interplay of these effects yields significantly enhanced inverted cell short-circuit current density (J_{SC}), fill factor (FF), and PCE. Unexpectedly, we also find that excessive **$PC_{71}BM$** in the **PBDB-TF:ITIC-Th** binary system alters the **PBDB-TF** orientation to π-edge-on, increases large scale **$PC_{71}BM$**-rich aggregations and BHJ upper surface **$PC_{71}BM$** composition. These morphology changes increase parasitic decay processes such as intersystem crossing from photoexcited **$PC_{71}BM$**, compromising the J_{SC}, FF, and PCE metrics. **ITIC-Th** X-ray diffraction reveals a unique sidechain-dominated molecular network with

previously unknown sidechain-end group stacking, rationalizing the STEM and GIWAXS results, photophysics, and the high μ_e. DFT computation reveals charge transfer networks within **ITIC-Th** crystallites, supporting excited-state electron delocalization from **ITIC-Th** to **$PC_{71}BM$**. This structure-property understanding leads to a newly reported NFA blend with PCE near 17 %.

Introduction

Solar energy is one of the most powerful renewable energy sources, with the potential to satisfy increasing global energy needs. It can be efficiently harvested and utilized by photosynthesis in plants, solar fuels, catalysts, and artificial electronic devices such as organic polymer solar cells (PSCs), which have shown power conversion efficiency (PCE) up to 19 % in the laboratory.[1] Traditional inorganic semiconductor photovoltaic devices made from silicon, colloidal nanocrystal, and copper indium gallium selenide (CIGS) materials, showing high PCE in the range of 20 % to 21 %[2], have been commercialized, and have dominated the solar cell market for decades.[3] Among them, pure crystalline silicon solar cells are approaching their PCE limit, and new semiconducting materials and techniques are becoming crucial. Compared with perovskite solar cell materials,[4] organic semiconductor technologies that use chemically synthesized polymers or small molecules with π-conjugated electrons as the charge carrier offer the attractions of earth-abundant starting materials, structure and property tunability *via* "green" chemical reactions,[5] large-area solution processability, light weight, minimal toxicity, and mechanical flexibility, which together make PSCs ideal as one of the next generation of solar energy harvesting technologies.[6-8]

PSCs[9] are commonly fabricated from solution-spin-coated bulk heterojunction (BHJ) films of small molecule, polymer, or polymer-small molecule blends as the photon absorbing active layer.[10] They enable PCEs that have steadily increased to a current 19 %,[7, 11, 12] due to the recent advent of new nonfullerene acceptor (NFA) small molecule materials.[13, 14] The PCE of a typical PSC is

determined by the open-circuit voltage (V_{OC}), short-circuit current density (J_{SC}), and fill factor (FF): PCE = $V_{OC} \times J_{SC} \times FF / P_{in}$, where P_{in} is the incident solar light power. Since PSC laboratory PCE values tend to be lower preceding optimization and manufacture, current leading research directions in the field remain focused on fundamental mechanistic studies supporting the chemical design and synthesis of new high-performing materials for device engineering and stability testing.[15]

In 2013, Friend and co-workers showed that the lowest-energy molecular triplet exciton (T_1) of the donor polymer is frequently lower in energy than the intermolecular charge transfer (CT) state, and the formation of triplet excitons can be the dominant loss mechanism in polymer-fullerene photovoltaic cells.[16] Recently, the same group reported that the majority of charge recombination under open-circuit conditions proceeds via the formation of non-emissive NFA triplet excitons.[17] Salleo and co-workers proposed a unified model of how charge carriers travel in conjugated polymer films, and showed that short-range intermolecular aggregation is sufficient for efficient long-range charge transport.[18] Regarding BHJ morphology and the Flory-Huggins parameter χ, in 2018, Ade and co-workers established a quantitative constant-kink-saturation relation between the temperature-dependent effective amorphous-amorphous interaction parameter $\chi_{aa}(T)$ and FF in organic solar cells.[19] Nevertheless, a clear relationship between BHJ morphology structure, photophysics, and device performance is still lacking in polymer-nonfullerene binary and polymer-nonfullerene-fullerene ternary systems.[20-22] Specifically, there are unanswered questions, such as: What is the highest performing BHJ film morphology, molecular orientation, semiconductor phase separation, and domain size possible? How do charge photogeneration and recombination influence V_{OC}, J_{SC}, and FF? How do free charge carriers recombine? To address these fundamental issues, our aim here is to provide a clearer picture of

the chemical structure, BHJ morphology, charge dynamics, and device performance correlations for BHJ devices containing *both* NFAs and fullerenes.

PBDB-TF (Figure 1a, also known as **PM6**) is a well-established, wide optical bandgap, semi-crystalline donor polymer,[23, 24] delivering high PCEs (7.4 % to 18 %) when matched with diverse NFAs,[7, 13, 25] and is chosen here to probe generalizable structure-performance correlations. **ITIC-Th** (Figure 1a) is a typical indacenodithienothiophene (**IDTT**)-based semi-crystalline electron acceptor with four 2-thienyl groups as the out-of-plane bulky non-conjugated part,[26] showing stronger optical absorption, higher electron mobility and PCE in organic semiconducting material blends than **ITIC**.[27] **BTBOL4F** is a typical **Y6**-based end-capping group extension and halogenation electron acceptor, showing a smaller optical bandgap, lower reorganization energy, larger electronic couplings, and a higher PCE than **Y6**,[28] and is chosen here to generalize the ternary strategy found in the **ITIC-Th** system. Note that some previously published results for **PBDB-TF**:**BTBOL4F** binary blend used a different **PBDB-TF** polymer batch than this work,[28] so the new polymer batch data for **PBDB-TF**:**BTBOL4F** will be included and compared in the analysis of ternary blends. Here, the photovoltaic parameters are measured in inverted solar cells, and space-charge-limited current (SCLC) mobilities are measured in single carrier diodes. BHJ film morphology is characterized by AFM, TEM, STEM, grazing incidence 2θ X-ray diffraction (GIXRD), two-dimensional grazing-incidence wide-angle X-ray scattering (2D-GIWAXS), resonant soft X-ray scattering (RSoXS), and near edge X-ray absorption fine structure spectroscopy (NEXAFS) measurements. Charge photogeneration and recombination dynamics are quantified by transient absorption (TA) spectroscopy and light intensity dependence experiments. Single crystal X-ray diffraction, together with density functional theory (DFT) analyses, reveal the intricate structural relationships between molecular packing and electronic properties such as

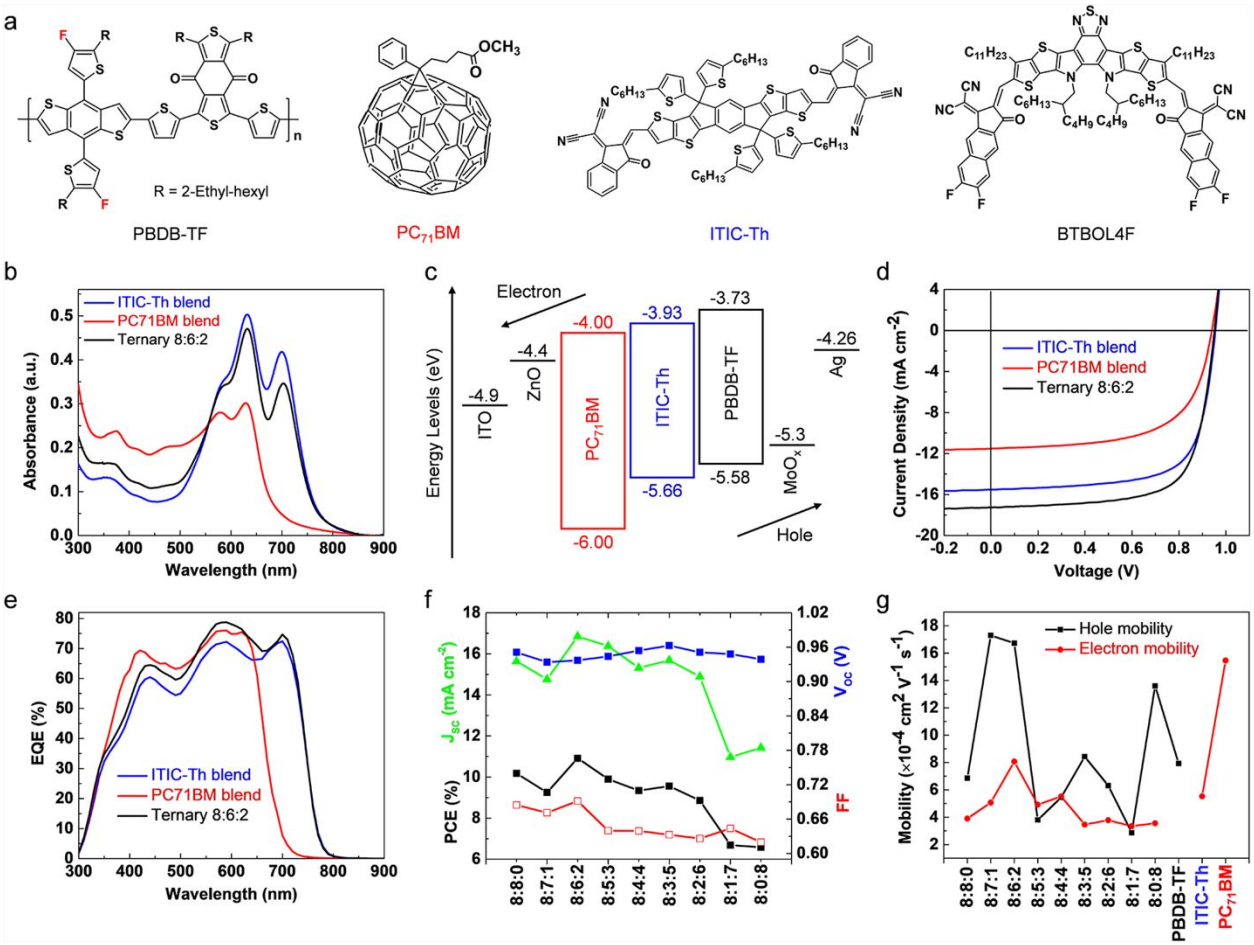

Figure 1. Organic semiconductors and electronic diode metrics. a, Chemical structures of **PBDB-TF**, **$PC_{71}BM$**, **ITIC-Th**, and **BTBOL4F**. **b**, Optical absorption spectra of binary and ternary blend films. **c**, Energetics of the semiconductors in the inverted PSC architecture used in this study.[26, 29, 30] **d**, Champion *J-V* characteristics and **e**, corresponding blend EQE spectra. **f**, Average photovoltaic parameters V_{OC}, J_{SC}, FF, and PCE as a function of binary and ternary blend composition. The corresponding standard deviation uncertainties are shown in Table 1. **g**, Average SCLC μ_h and μ_e values of neat and blend films as a function of binary and ternary blend composition. The corresponding standard deviation uncertainties are shown in Table 1. Blend composition is denoted by mass fraction (in %) of **PBDB-TF:ITIC-Th:$PC_{71}BM$**.

reorganization energy, electronic coupling, charge delocalization, and excited-state energetics. These generalizable understandings can then be applied to other NFA systems to ultimately enhance PSC performance. Overall, we believe that this contribution provides general quantitative multiple structure-property-device performance design rules and high PCE design paradigms for future PSC development.

Results and Discussion

We begin by blending the donor polymer **PBDB-TF**, having good molecular mass and polydispersity (Figure S1) with the small molecule acceptor semiconductors **ITIC-Th** and **$PC_{71}BM$**. The resulting binary and ternary films are characterized in inverted PSC architectures, hole-only and electron-only single carrier diodes, and the film morphology, charge photogeneration and recombination are quantified by a diverse range of high-resolution spatial and temporal experimental techniques. For evaluating solid-state packing and theoretical understanding, single crystal structure analysis of **ITIC-Th** is reported,[31] shedding light on the high-performance mystery of this NFA material. In this discussion, we organize the flow sequentially from solar cell fabrication and performance, charge carrier mobility, BHJ film morphology characterizations, GIWAXS, NEXAFS, single crystal structure analysis, and RSoXS experiments, to charge photogeneration and recombination dynamics, and theoretical simulations. All experimental details are provided in the Supplementary Information (SI).

Solar cell fabrication and performance

Photovoltaic performance was characterized in the inverted device architecture, ITO (indium tin oxide)/ZnO (zinc oxide)/Photoactive layer/MoO_x (molybdenum oxide)/Ag (Figure 1c) under AM 1.5G illumination at 100 mW cm^{-2}. The ZnO electron extraction (hole blocking) interfacial layer was deposited using the sol-gel method,[29] while the MoO_x hole extraction (electron blocking) layer was thermally grown under vacuum.[32] More experimental details of the device fabrication and measurements can be found in the SI. Figure 1d,e shows the champion current density versus voltage (*J-V*) characteristics and corresponding external quantum efficiency (EQE) spectra, respectively, and Table 1 summarizes all the binary and ternary BHJ electronic device metrics.

PBDB-TF:ITIC-Th binary cells were first optimized by tuning the polymer concentration, solvent additive, annealing temperature and time (see SI for details, Table S2), and the optimal BHJ films were spin-coated using chloroform solutions of **PBDB-TF** and **ITIC-Th** in a 1:1 mass ratio without additives, and annealed at 160 °C for 5 min. The result shows an average J_{SC} of 15.64 mA cm^{-2}, V_{OC} of 0.951 V, and FF of 0.68, yielding an average PCE of 10.18 % (10.42 % champion, Table 1), comparable to previous reports.[33] For comparison, **PBDB-TF:PC$_{71}$BM** binary cells output an average PCE = 6.58 % (6.77 % champion).[29] The solar cell V_{OC} values of **PBDB-TF:ITIC-Th** and **PBDB-TF:PC$_{71}$BM** agree with the LUMO depth of acceptors from thin film cyclic voltammetry (CV)[26, 29, 30] as shown in Figure 1c. Ternary BHJ solar cells were next fabricated retaining the optimized **PBDB-TF:ITIC-Th** binary conditions (see SI for details), revealing first a decrease, then an increase and finally a fall in PCE as the **PC$_{71}$BM** content is increased and the **ITIC-Th** content is decreased (Figure 1f). This trend mainly reflects J_{SC} and FF changes, since the V_{OC} values are almost unchanged. The optimized weight ratio of **ITIC-Th** to **PC$_{71}$BM** is found to be 6:2, and the blend exhibits an average J_{SC} = 16.85 mA cm^{-2}, V_{OC} = 0.937 V, FF = 0.69, and PCE = 10.92 %. The champion PCE achieved for this composition is 11.55 %, among the highest values achieved in similar PSC systems.[34, 35] The PCEs of the **8:8:0**, **8:7:1**, **8:5:3**, **8:4:4**, **8:3:5**, and **8:2:6** blend compositions (**PBDB-TF:ITIC-Th:PC$_{71}$BM**) are found to be rather similar, ranging from 9.49 % to 10.42 %, and significantly higher than those of the **8:1:7** ternary and **PBDB-TF:PC$_{71}$BM** binary blends (Table 1, Figure S5). A similar PCE trend is also reported for a **Y6**-derivative ternary system with **BTBOL4F (**Figure S7, Table S5), **PBDB-TF:BTBOL4F:PC$_{71}$BM**, with PCEs approaching 17 % realized for the first time in the **8:7:1** and **8:6:2** blends[28] and suggesting a wide applicability of this ternary strategy.

Table 1. PSC performance and charge transport data for binary and ternary blends

Blend[a]	Solar Cell					Single Carrier Diode		
	V_{OC} (V)	J_{SC} (mA cm^{-2})	FF (%)	PCE (%)	EQE J_{SC} (mA cm^{-2})	μ_h (10^{-4} cm^2 V^{-1} s^{-1})	μ_e (10^{-4} cm^2 V^{-1} s^{-1})	μ_h/μ_e
8:8:0	0.951±0.004 (0.954)	15.64±0.24 (15.52)	68.45±1.02 (70.40)	10.18±0.17 (10.42)	14.97	6.86 ± 3.73	3.90 ± 2.59	1.76
8:7:1	0.934±0.005 (0.935)	14.76±0.47 (15.46)	67.11±0.59 (66.99)	9.25±0.29 (9.68)	14.47	17.29 ± 2.25	5.07 ± 3.45	3.41
8:6:2	0.937±0.005 (0.950)	16.85±0.60 (17.26)	69.15±0.68 (70.43)	10.92±0.45 (11.55)	16.00	16.73 ± 7.98	8.07 ± 7.05	2.07
8:5:3	0.944±0.005 (0.952)	16.38±0.27 (16.52)	63.97±0.83 (65.36)	9.90±0.24 (10.27)	15.77	3.80 ± 0.63	4.92 ± 3.32	0.77
8:4:4	0.954±0.006 (0.963)	15.32±0.31 (15.62)	63.94±0.25 (64.15)	9.34±0.22 (9.65)	15.10	5.45 ± 2.20	5.52 ± 4.57	0.99
8:3:5	0.963±0.010 (0.964)	15.69±0.48 (15.81)	63.26±1.79 (64.67)	9.56±0.47 (9.86)	15.35	8.43 ± 2.53	3.46 ± 2.40	2.44
8:2:6	0.951±0.008 (0.947)	14.89±0.58 (15.64)	62.60±1.46 (64.09)	8.86±0.36 (9.49)	15.00	6.32 ± 0.77	3.78 ± 2.74	1.67
8:1:7	0.948±0.006 (0.948)	10.97±0.38 (11.32)	64.36±0.90 (64.70)	6.69±0.21 (6.94)	11.14	2.87 ± 0.71	3.35 ± 2.40	0.86
8:0:8	0.929±0.006 (0.939)	11.43±0.29 (11.52)	61.98±0.58 (62.56)	6.58±0.16 (6.77)	12.42	13.60 ± 6.42	3.56 ± 1.95	3.82
8:7:1	0.856±0.005 (0.861)	26.60±0.51 (27.11)	70.21±0.83 (71.1)	16.11±0.49 (16.6)	26.1	/	/	/
8:6:2	0.855±0.004 (0.859)	26.55±0.60 (27.10)	70.58±0.60 (72.2)	16.25±0.46 (16.7)	26.2	/	/	/

[a]Blend films were prepared in a mass ratio of **PBDB-TF:ITIC-Th:PC$_{71}$BM** (the top nine lines) and **PBDB-TF:BTBOL4F:PC$_{71}$BM (**the bottom two lines, EQE J_{SC}s were calculated from the inverted cells). Average values are from ≥ 6 separate PSC devices. Values in parenthesis are for champion solar cells. Average SCLC mobilities obtained from ≥ 5 separate diodes. Standard deviation values for each parameter as given as ± values. Solar cell and single carrier diode device performance of analogous **PBDB-TF:PC$_{71}$BM** BHJ films is from ref[29] for comparison.

Interestingly, the EQE spectra of the **PBDB-TF:ITIC-Th**, **PBDB-TF:PC$_{71}$BM** blends show strong photoresponse from λ = 300 nm to 800 nm, and 300 nm to 750 nm, respectively (Figure 1e). The greater **ITIC-Th** optical absorption range relative to **PC$_{71}$BM** results in a greater J_{SC} (15.52 versus 11.52 mA cm^{-2}). Notably, the ternary **8:6:2** blend exhibits similar EQE response as

the binary **PBDB-TF:ITIC-Th** blend with enhanced EQE from 350 nm to 675 nm (**PBDB-TF** optical absorption) and 680 nm to 740 nm (**ITIC-Th** optical absorption) wavelength range. Overall, the EQE spectra (Figure S5) are in very good agreement with the corresponding PSC *J-V* data (Table 1).

Single carrier diode and charge carrier mobility

In general, the carrier mobility contributes significantly to J_{SC}, FF, and PCE metrics. To understand this, the vertical charge transport in the present thin films was investigated by the single carrier diode SCLC method (Table 1, Figure 1g, see the SCLC measurements section in SI for details).[36, 37] Hole mobilities (μ_hs) were measured using ITO/MoO_x/organics/MoO_x/Ag diodes, and electron mobilities (μ_es) were measured using ITO/ZnO/organics/LiF/Al diodes, respectively. As a control, the neat **PBDB-TF**, **ITIC-Th**, **$PC_{71}BM$** films were found to have electron mobilities of [$(7.93 \pm 1.31) \times 10^{-4}$, $(5.53 \pm 3.74) \times 10^{-4}$, and $(15.46 \pm 11.54) \times 10^{-4}$] $cm^2\ V^{-1}\ s^{-1}$, respectively, similar to literature reports.[26, 38, 39] These suggest the present measurements are reliable, despite the estimated uncertainties. Binary **PBDB-TF:ITIC-Th** blend films have $\mu_h = (6.86 \pm 3.73) \times 10^{-4}$ $cm^2\ V^{-1}\ s^{-1}$ and $\mu_e = (3.90 \pm 2.59) \times 10^{-4}$ $cm^2\ V^{-1}\ s^{-1}$, comparable to other NFA-based blends with high PCEs.[25, 40] Interestingly, in comparison, the present binary **PBDB-TF:$PC_{71}BM$** blend films exhibit higher $\mu_h = (13.60 \pm 6.42) \times 10^{-4}$ $cm^2\ V^{-1}\ s^{-1}$ but similar $\mu_e = (3.56 \pm 1.95) \times 10^{-4}$ $cm^2\ V^{-1}\ s^{-1}$.[29] This μ_h enhancement is consistent with fullerene-induced **PBDB-TF** π-edge-on ordering in the blend vs neat **PBDB-TF** (*vide infra*). Comparing all the binary and ternary blend films, the ternary **8:6:2** films have the highest $\mu_h = (16.73 \pm 7.98) \times 10^{-4}$ $cm^2\ V^{-1}\ s^{-1}$ and highest $\mu_e = (8.07 \pm 7.05) \times 10^{-4}$ $cm^2\ V^{-1}\ s^{-1}$, which should be beneficial for FC extraction to the electrodes during PSC operation. The μ_hs of the ternary **8:5:3**, **8:4:4**, **8:3:5**, **8:2:6**, **8:1:7**, and binary **PBDB-TF:ITIC-Th** blend films are of similar magnitude, 10^{-4} $cm^2\ V^{-1}\ s^{-1}$, and the μ_es of all binary and ternary blends follow

the interesting trend of first increasing and then falling with increasing **$PC_{71}BM$** content (Figure 1g), reflecting the acceptor composition ratio, BHJ phase separation, and acceptor molecular packing in the BHJs (*vide infra*).

AFM, TEM, and STEM characterization

Similar to most light-harvesting biological systems and natural photosynthesis, the active layer film microscopic structure of photovoltaic devices is known to play a key role in exciton photogeneration and dissociation, free charge carrier transport and recombination, and the resulting device performance. In the present case, introducing **$PC_{71}BM$** into the binary **PBDB-TF:ITIC-Th** system makes this role more intriguing. Previously, only limited quantitative understanding of molecular orientation and crystalline packings in organic semiconductor blends was available,[29, 41] with less clarity for amorphous domains.[18, 19, 29, 42] Next, the photoactive layer BHJ morphology of the present films was comprehensively investigated by AFM, TEM, STEM microscopy, and by GIXRD, GIWAXS, NEXAFS, RSoXS X-ray experiments.

Typical tapping mode AFM images of **PBDB-TF:ITIC-Th**, **PBDB-TF:$PC_{71}BM$**, and **8:6:2** ternary blends (Figure S12) show RMS surface roughness, R_q of (1.30 nm, 0.81 nm, and 1.54) nm, respectively, indicating a relatively smooth upper surface for these blend films. They also display similar phase images. TEM in the bright field imaging mode was next used to probe bulk film morphology and visualize spatial domain distributions. Due to the greater electron density and crystallinity of the acceptor molecules than in **PBDB-TF**, the lighter and darker regions in the bright field mode TEM images are assigned to **PBDB-TF** and acceptor domains, respectively (Figure S14).[43] The **PBDB-TF:ITIC-Th** blend exhibits features with randomly distributed **ITIC-Th** domains, while the **PBDB-TF:$PC_{71}BM$** blend exhibits extensive **$PC_{71}BM$** aggregation. This result is consistent with the definitive spectroscopic observation of long-range charge separation

distances ≥ 4 nm in organic semiconductor photovoltaic diodes by Friend *et al*.[44] The smaller **ITIC-Th** domains in the **PBDB-TF:ITIC-Th** blend which exhibit good phase separation correlate with more efficient charge separation and superior device performance than the **PBDB-TF:PC$_{71}$BM** blend (10.42 % versus 6.77 %, Table 1). In marked contrast, the ternary **8:6:2** blend clearly exhibits a well-balanced interpenetrating network (Figure S14). Thus, incorporating an optimal level of **PC$_{71}$BM** facilitates a better balanced distribution of polymer/acceptor domains in the blend film, probably limiting geminate recombination and spatially facilitating exciton scission and solar cell performance.

The typical low-angle annular dark field (LAADF)-STEM images from the **PBDB-TF:ITIC-Th**, ternary **8:6:2**, **8:3:5**, and **PBDB-TF:PC$_{71}$BM** blends are shown in Figure 2a-d and S16. In this LAADF mode, the brighter regions correspond to higher mass-thickness, which is complementary to the TEM bright field mode. The power spectral density (PSD) profiles calculated from the images are shown in Figure S17. The peak in the PSD profiles observed for all the samples corresponds to a size scale of ~15 nm and matches the center-to-center distances of fibrillar structures in the micrographs. Since this feature occurs in all the samples, including the **PBDB-TF:PC$_{71}$BM** blend, it likely originates from the **PBDB-TF** fibrils. In the blends with **ITIC-Th** as major component we see crystallites that are likely **PBDB-TF** as well as **ITIC-Th**. This is consistent with the semi-crystalline nature of **PBDB-TF** and **ITIC-Th**, which is also evident in the GIXRD and GIWAXS measurements (*vide infra*). As the fullerene content is increased, finer size scales are observed in the **8:3:5** ternary, and with further **PC$_{71}$BM** addition, the domain sizes are seen to increase again in the binary **PBDB-TF:PC$_{71}$BM** sample. Overall, the TEM data generally agree with the STEM results.

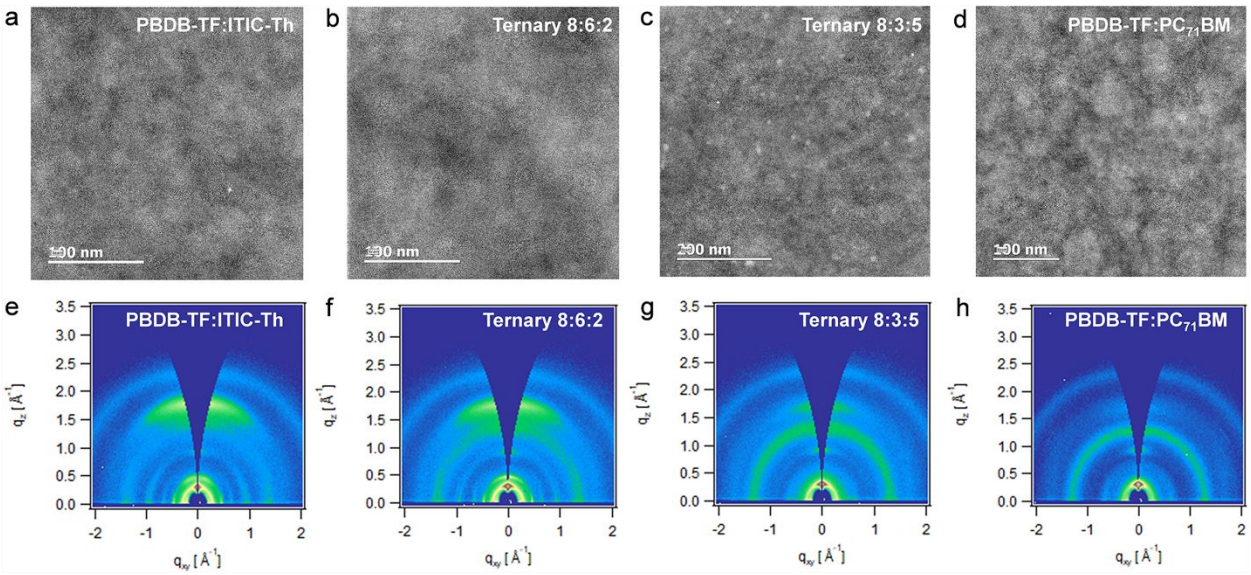

Figure 2. STEM and GIWAXS results. LAADF-STEM images and corresponding 2D GIWAXS patterns of **a**,**e**, **PBDB-TF:ITIC-Th** binary, **b**,**f**, ternary **8:6:2**, **c**,**g**, ternary **8:3:5**, **d**,**h**, **PBDB-TF:PC$_{71}$BM** binary blends.

GIWAXS and NEXAFS analysis

Since the present BHJ films are highly nano-crystalline, GIWAXS together with single crystal X-ray diffraction are the obvious experimental techniques to provide molecular crystalline packing information for neat and BHJ films.[29, 45] The GIWAXS measurements were conducted to further quantify the crystalline packings of the **PBDB-TF** and acceptor domains in these blend films. The 2D GIWAXS patterns of the binary and ternary blends are shown in Figure 2e-h. The out-of-plane (OoP) and in-plane (IP) 1D sector-averaged profiles obtained from OoP and IP sectors from blends and neat films are shown in Figure S21. Some interesting trends are observed from this dataset. For all the blend samples, the **PBDB-TF** (100) lamellar stacking near q = 0.3 Å^{-1} and (010) π-π stacking peak near 1.7 Å^{-1} can be seen in both OoP and IP directions, suggesting presence of π-face-on as well as π-edge-on populations. Pole figures (Figure S20) calculated from the **PBDB-TF** (100) lamellar stacking peak near 0.3 Å^{-1} in the GIWAXS data further indicate that **PBDB-TF** is predominantly π-edge-on in the neat film and **PBDB-TF:PC$_{71}$BM** binary blend, and exhibits a monotonic change towards increasingly π-face-on orientation with increasing **ITIC-Th** content.

Diffraction strengths (DS) calculated from the integration of the pole figures show that the **PBDB-TF** ordering is greater in the blends than in the neat sample. **PBDB-TF** is found to have ≈20 % higher DS in the ternary samples while similar values are found in both the **PBDB-TF:ITIC-Th** and **PBDB-TF:$PC_{71}BM$** binary blends. The polymer OoP (100) lamellar stacking coherence lengths (calculated with the Scherrer equation; see SI) are found to be higher in blends compared to the neat polymer or with **ITIC-Th**, suggesting larger crystallites in accordance with the higher DS values of the blend samples. However, in the binary and ternary blends, the OoP coherence lengths appear unaffected by the blend composition. The polymer IP (100) coherence is found to slightly increase with increasing **$PC_{71}BM$** content, suggesting the presence of slightly larger face-on **PBDB-TF** crystallites. The coherence lengths then fall with further **$PC_{71}BM$** addition (sample **8:2:6** onwards). **ITIC-Th** ordering peaks are also observed in the diffraction patterns. The **ITIC-Th** GIWAXS peaks are indexed by analogy with the single crystal indexing for consistency. Pole figures calculated from the **ITIC-Th** (00l) lamellar stacking peak near 0.47 $Å^{-1}$ indicate presence of π-face-on **ITIC-Th** crystallites. DS calculated from the integration of the pole figures and corrected for **ITIC-Th** content show that the **ITIC-Th** ordering in binary **PBDB-TF:ITIC-Th** is retained after adding small amounts of **$PC_{71}BM$** but decreases with further **$PC_{71}BM$** addition (Figure 3a). **ITIC-Th** lamellar ordering peaks are not observed for blends where **$PC_{71}BM$** is the major acceptor component *e.g.*, the **8:3:5**, and **8:2:6** blends, implying that **$PC_{71}BM$** addition results in decreased **ITIC-Th** ordering. Note also that both IP and OoP coherence lengths are higher in the ternary samples suggesting presence of larger **ITIC-Th** crystallites in ternary versus binary blends. A more complete picture is obtained from the **PBDB-TF** (010) and **ITIC-Th** π-π (h00) OoP stacking peaks observed in the **PBDB-TF:ITIC-Th** binary and ternary samples. While the polymer (010) coherence length remains almost unchanged (Figure 3a), the **ITIC-Th**

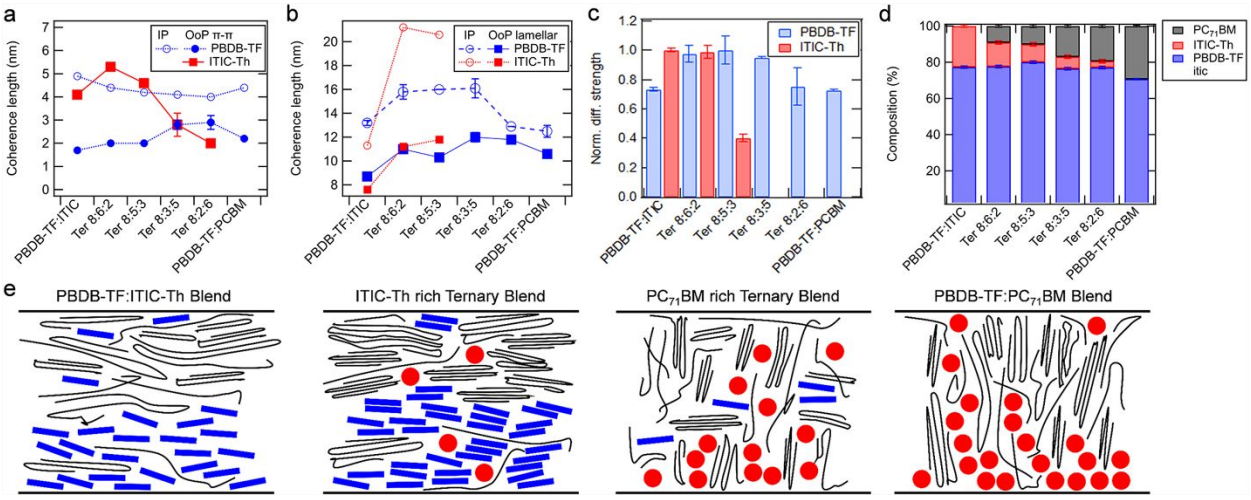

Figure 3. GIWAXS, NEXAFS analysis, and molecular packing models for the present binary and ternary BHJ blends. a, IP and OoP coherence lengths of **PBDB-TF** and **ITIC-Th**, **b,** π-π stacking and lamellar stacking peaks, **c**, relative diffraction strength for **PBDB-TF** and **ITIC-Th** calculated from lamellar diffraction peak in 2D GIWAXS patterns of binary and ternary blends, **d**, surface composition from fits to magic angle (54.7°) PEY NEXAFS spectra from binary and ternary blends using spectra from neat samples. Coherence length error bars are standard deviations from multi-peak fitting of 1D GIWAXS scattering profiles. Diffraction strength error bars are proportional to uncertainties in film thickness measurements. Surface composition errors are standard deviation values from fits to the NEXAFS spectra. **e**, schematic illustration of BHJ film morphology (side view). Black wires refer to **PBDB-TF**, blue bars refer to **ITIC-Th** molecules, and red circles refer to **$PC_{71}BM$**.

(h00) OoP coherence exhibits a trend that is qualitatively similar to the lamellar coherence lengths *i.e.*, an initial increase with **$PC_{71}BM$** addition with the maximum value observed for the **8:6:2** sample, and then a gradual decrease with further increase of **$PC_{71}BM$** content. The polymer (100) lamellar spacing in both IP and OoP direction is maximum for the **PBDB-TF:ITIC-Th** binary blend sample and then falls monotonically from 21.5 Å to 20.7 Å as the blend **$PC_{71}BM$** content increases. In contrast, the **ITIC-Th** (00l), polymer, and **ITIC-Th** π-π *d*-spacings are found to be essentially unaffected by blend composition. Overall, the molecular orientation, stacking distance, crystalline information obtained from the GIWAXS measurements is largely consistent with the GIXRD data (see details in SI), AFM, and STEM results. The molecular orientation and vertical phase separation of the crystalline domains in the binary and ternary BHJ films are illustrated in

Figure 3e. In **PBDB-TF:ITIC-Th** blends, **PBDB-TF** and **ITIC-Th** exhibit mainly π-face-on orientation. The optimal incorporation of **$PC_{71}BM$** into **PBDB-TF:ITIC-Th** binary system retains the original π-face-on molecular orientation and crystallinity. As the **$PC_{71}BM$** content is increased in ternary systems, excessive incorporation of **$PC_{71}BM$** into **PBDB-TF:ITIC-Th** alters **PBDB-TF** orientation to π-edge-on relative to electrode, decreases **ITIC-Th** crystallinity, and increases large scale **$PC_{71}BM$** aggregations. In **PBDB-TF:$PC_{71}BM$** blend, **PBDB-TF** exhibits π-edge-on orientation with **$PC_{71}BM$**-induced polymer crystallization.

Surface-sensitive NEXAFS spectroscopy was next employed to quantify the composition of the BHJ top surface. All samples show a polymer-rich top surface (Figure 3d), similar to our previous observations in amorphous polymer-semi-crystalline acceptor BHJ **PBDT(Ar)-FTTE:ITIC-Th**[5] and semi-crystalline polymer-crystalline acceptor BHJ **PBDB-TF:Y6**[41] films. This unique vertical phase separation is beneficial to the inverted solar cell structure implemented here. The polymer enrichment is slightly lower in the **PBDB-TF:$PC_{71}BM$** binary (70 %) compared to the binary **PBDB-TF:ITIC-Th** or the ternary samples, and the BHJ upper surface composition of different blend films are shown in Figure 3d. The trend in surface composition also indicates that **PBDB-TF** has a lower miscibility with **ITIC-Th**, as compared to **$PC_{71}BM$**, which is also in accord with the RSoXS results (*vide infra*).

Single crystal X-ray diffraction

Molecular single crystal packing provides insight into how molecules organize in a thermal environment, and can assist in understanding **ITIC-Th** nanoscale molecular packing,[29] charge separation, charge transport properties[46] in neat and BHJ blend films, especially for the crystalline domains in films.[7, 8, 47-49] Previously, we observed short π-π distances between end-groups/cores in **IT(z)N-C9**,[29] **ITIC-nF**,[46] **IT(z)N-F4**,[50] and **Y6**[41] acceptor crystals, and found this kind of π-face-

on packing in crystalline domains of spin-coated neat and BHJ films. Considering the currently limited **ITIC-Th** single crystal data reported in literature,[31, 51] single crystals of **ITIC-Th** were grown here by diffusing acetone vapor into dibromomethane solution (see SI for details). **ITIC-Th** molecules crystallize in a triclinic unit cell (deposited CCDC No. 2181313) with a = 8.7612(11) Å, b = 13.2409(16) Å, c = 17.624(2) Å, α = 93.211(6)°, β = 98.646(6)°, γ = 97.221(6)°, different from the previously reported monoclinic polymorph.[31] In the present results, the thiophene ring and long alkyl side chain stretch between molecular layers. Similar to most IC-based NFAs,[52] the

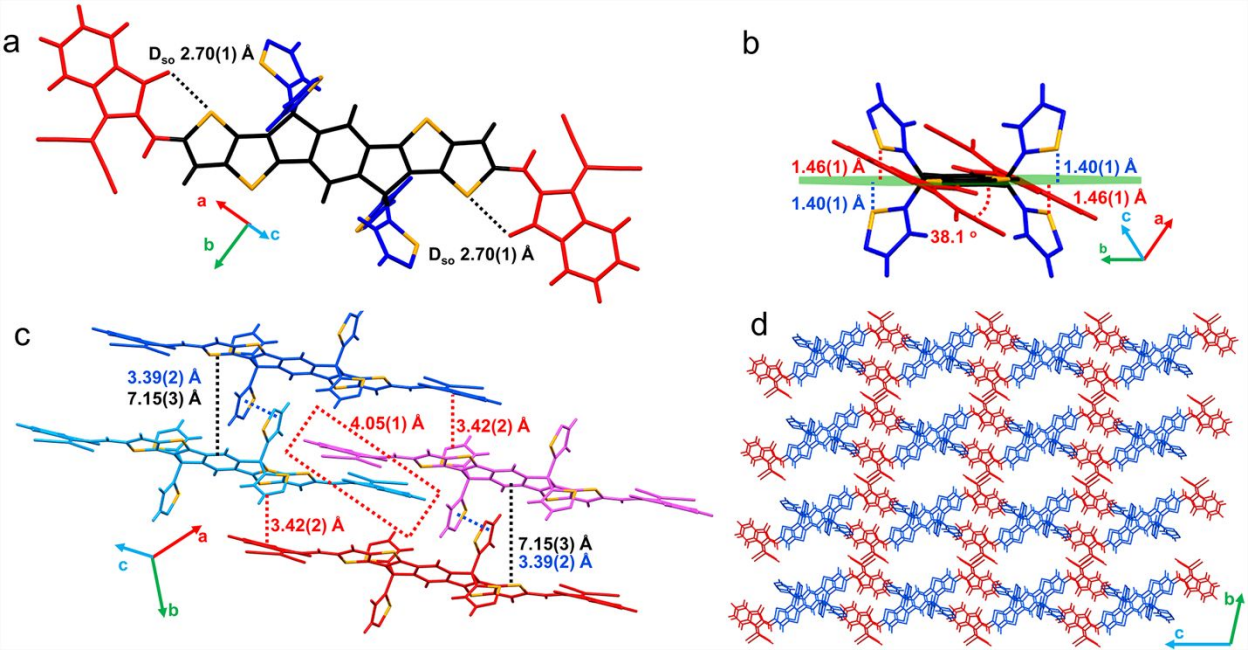

Figure 4. ITIC-Th single crystal visualization. a, Monomolecular **ITIC-Th**, sulfur-oxygen conformational locking and the interaction distance (D_{so}); **b**, Monomolecular visualization along the plane of the IT backbone; **c**, Unit cell of the **ITIC-Th** molecule and the π-π stacking distance with the estimated deviations in parentheses; **d**, **ITIC-Th** stacking pattern viewed along the *a*-axis.

sulfur···oxygen conformational locks[51, 53] are also found in **ITIC-Th**. But interestingly within the crystal network of **ITIC-Th**, end group (EG) – EG stacking (Figure 4d) is only present at the edge of the unit cell through the stacking of two malononitrile groups (Figure 4c-d, red dot rectangle, 3.49 Å), which is uncommon in other **ITIC**-based NFAs in which the stackings mostly involve

the aromatic regions.[46] As such, the computed electronic couplings (*vide infra*) suggest the EG-EG couplings (10 meV) in the **ITIC-Th** crystal networks are smaller than in other **ITIC**-based NFAs.

In contrast to most other IT-based NFAs, the interaction distance between the oxygen atom of the IC EG and the sulfur atom of the thiophene unit (D_{so}, Figure 4a) of the **ITIC-Th** is 2.70 Å, larger than in most other **ITIC**-based NFAs,[46] indicating a weak intramolecular planarity of **ITIC-Th** (Figure 4a). Confirmed by viewing along the IT-backbone plane in the crystal network (Figure 4b, green plane), the EG is tilted 38.1° from the plane of the IT-backbone. Along with the absence of EG-EG stacking in **ITIC-Th**, the thiophene sidechain of **ITIC-Th** plays an essential role in organizing the crystal network of **ITIC-Th**. Surprisingly, two types of stacking motifs are observed in the **ITIC-Th** crystal network, 1) horizontal π-face-on sidechain-thiophene (sTh)-sTh stacking (Figure 4c, blue dot line, 3.39 Å); 2) vertical π-edge-on sTh-EG stacking (Figure 4c, red dot line, 3.42 Å). It is interesting that all four thiophene sidechains of each **ITIC-Th** molecule participate in forming these two types of stacking motifs. To confirm this observation, we calculated the distance from the S atom of the sidechain thiophene ring to the IT-backbone plane (Figure 4b). Two different distances are obtained, 1.46 Å for the sidechain with sTh-sTh stacking, 1.40 Å from the sidechain with sTh-EG stacking. This observation confirms that two types of atomic interaction influence the thiophene sidechain orientation, and thus all the thiophene sidechains of **ITIC-Th** participate in this stacking motif construction. Note that although most stacking motifs in the **ITIC-Th** crystal structure involve the thiophene sidechain, the **ITIC-Th** blends still deliver substantial photovoltaic performance. Considering that the highly twisted core-EG configuration is less favorable for electron transport,[54, 55] and the sidechain-based stacking does not exhibit strong computed electronic couplings, we hypothesize that the predominant

intermolecular **ITIC-Th** charge transport may be via unexpected malonitrile EG stacking of two **ITIC-Th** molecules, and transport proceeds via two unit cells. This hypothesis is supported by DFT modeling (*vide infra*).

Resonant soft X-ray scattering (RSoXS) analysis

RSoXS was next performed to quantify the phase separation size scales in the two binary blends as well as the ternary **8:6:2**, and **8:3:5** blend films. Note here that in case of binary blends there is only one material contrast function arising from the single pair of materials. However, for ternary

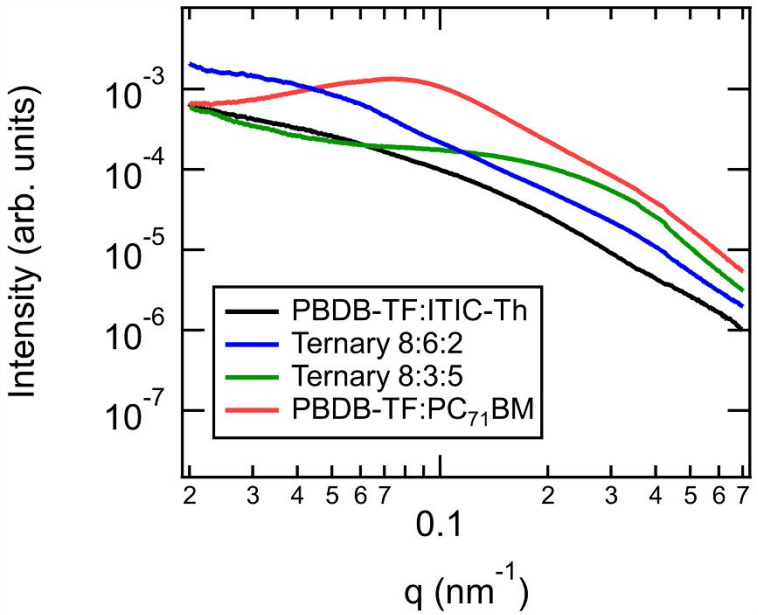

Figure 5. RSoXS 1-D profiles for binary and ternary BHJ blends. RSoXS profiles acquired at high polymer:acceptor material contrast energy of 284 eV from the **ITIC-Th** and **$PC_{71}BM$** binary, **8:6:2**, and **8:3:5** ternary blends.

blends the three different materials result in three different material contrast functions with different energy dependencies. The three material contrast functions are shown in Figure S25. In Figure 5, the 1D RSoXS profiles from the two binary and ternary **8:6:2** and **8:3:5** blends are shown. The peak positions and overall profile shapes for both **PBDB-TF:ITIC-Th** and **8:6:2** ternary blends suggest that the size scales present in the two systems are similar. For all the samples, a high-q peak at $q \approx 0.4$ nm^{-1} is observed, corresponding to a size scale of ≈ 15 nm, in excellent

agreement with the LAADF-STEM results if we interpret it as arising from a long period of polymer-rich domains. Additionally, a peak at a lower *q* value is observed for all the blends, and its position varies with blend composition. For binary **PBDB-TF:ITIC-Th** and ternary **8:6:2** samples, the low-*q* peak corresponds to large ≈ 150 nm to 200 nm-scale domains seen in LAADF-STEM images (Figure S16) that are likely **ITIC-Th**-rich. As blend **$PC_{71}BM$** content is increased, the low-*q* peak position falls to ≈ 0.15 nm^{-1} (size scale ≈ 40 nm) in ternary **8:3:5**, implying that besides affecting **ITIC-Th** crystallinity, **$PC_{71}BM$** addition also results in **ITIC-Th**-rich domain size reduction. The lower-*q* peak in the **8:3:5** blend likely arises from polymer:acceptor mixed regions. The position of the low-*q* peak again increases with further addition of **$PC_{71}BM$** to ≈ 0.08 nm^{-1} (size scale ≈ 80 nm) in the binary **PBDB-TF:$PC_{71}BM$** blend and likely arises from large scale **$PC_{71}BM$**-rich and/or polymer-**$PC_{71}BM$** mixed regions. Further analysis of the RSoXS data is not possible with currently available analysis frameworks because those methods assume two phases. For example, it is not appropriate to perform RSoXS "relative domain purity" estimations that are frequently correlated to device performance, because with a potential number of phases greater than two, changes in scattering intensity are ambiguous with respect to which phases or components are implicated. Contributions from orientation contrast and mass roughness are also possible. Even without orientation effects, and assuming three phases plus roughness creating a fourth vacuum phase, there are N*(N-1)/2 = 4*3/2 = 6 binary contrasts to consider. Model fitting of the RSoXS data will not yield reliable results since it is not clear which phases are responsible for which scattering features. We anticipate that the detailed energy dependence of RSoXS data might, in the future, support analysis frameworks that separate such effects.

Charge photogeneration and recombination dynamics

With a clear picture of solar cell and single carrier diode device performance, BHJ film morphology and molecular nanoscale packing, femtosecond transient absorption (fsTA) spectroscopy was next performed on the binary and ternary blends to determine the reason for differences in their efficiencies, therefore to strengthen the connection between BHJ film crystalline morphology, charge dynamics, and device performances. Following selective photoexcitation of **ITIC-Th** at λ = 720 nm, the rate of hole transfer from the **ITIC-Th** to **PBDB-TF** was monitored by the appearance of the ground state polymer bleach at λ = 580 nm (Figure 6). Excitation at λ = 720 nm was chosen to suppress the many possible photophysical pathways from the photoexcited polymer that can obscure the hole transfer dynamics. Since the acceptor bleach (ca. 700 nm) will be present for all populations of acceptor excited states regardless of their ability to charge transfer, monitoring the polymer bleach after selectively exciting **ITIC-Th** thus provides an unambiguous probe of the charge separation, while avoiding the overlapping signals associated with the acceptor excited-state and carrier photoinduced absorptions in the redder portions of the spectrum (>800 nm). Figure 6 shows that the rate of hole transfer in the **PBDB-TF:ITIC-Th** blend with a larger concentration of **$PC_{71}BM$** is significantly slower ($k_1 = 3.1 \times 10^{12}$ s^{-1}, Figure S29) than in the blends with a lower fullerene concentration ($k_1 = 4.5 \times 10^{12}$ s^{-1}, Figure S28). This likely reflects the high **$PC_{71}BM$** concentration reducing interfacial contact between the **ITIC-Th** and **PBDB-TF** domains (see Figure 3e). However, the hole transfer rates in the ternary **8:6:2** blend and the binary **PBDB-TF:ITIC-Th** blend are the same (Figures S27 and S29), but the charge collection efficiency is higher with the addition of small amounts of **$PC_{71}BM$** (Table 1). This may reflect the broader absorption of the blend in the UV region (Figure 1b) with the addition of **$PC_{71}BM$** and can be a result of a favorable BHJ film morphology, as confirmed in the TEM, STEM, GIWAXS, and RSoXS measurement sections. The difference in device performance between the

8:6:2 ternary mixture and that with no **$PC_{71}BM$** strongly suggests that the effects are morphological in nature since the addition of the fullerene does not affect the energetics of the **PBDB-TF:ITIC-Th** pair, and absorption of **$PC_{71}BM$** at 720 nm is very small and will not significantly contribute to the initial charge separation. Moreover, this photophysics-morphology

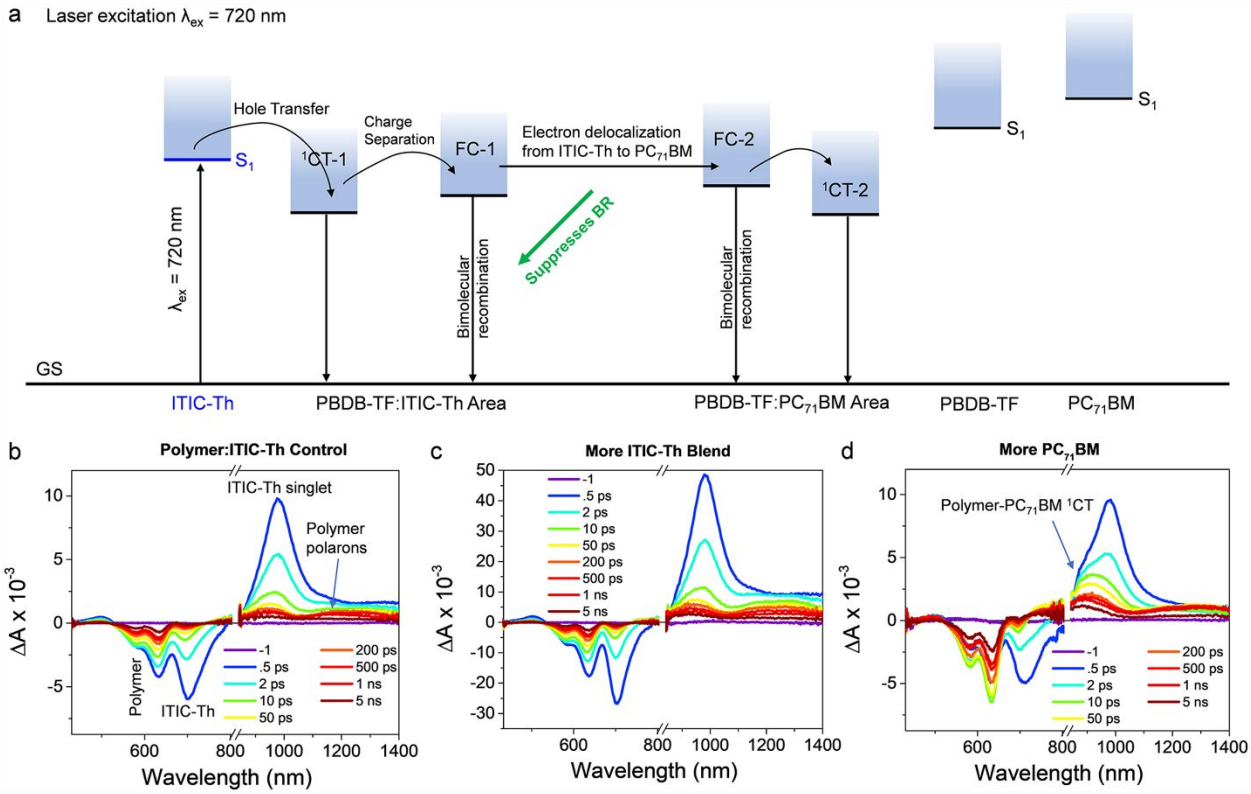

Figure 6. Photophysics model and TA spectroscopy of the indicated BHJ blends. a, The proposed photophysical process in current PSC systems under 720 nm laser excitation. fsTA spectra of **b**, **PBDB-TF:ITIC-Th** binary, **c**, **8:6:2** ternary, **d**, **8:3:5** ternary blend films.

relation in the **PBDB-TF:ITIC-Th:$PC_{71}BM$** system is also observed in the **PBDB-TF:BTBOL4F:$PC_{71}BM$** systems. In the **BTBOL4F**-based binary and ternary blends, the TA data for the **PBDB-TF:BTBOL4F** binary blend excited at λ = 830 nm show ultrafast hole transfer to the polymer, with the **PBDB-TF** bleach intensifying with a rate constant of $k_1 \sim 3 \times 10^{12}$ s^{-1} (Figures S37). Note that the TA data on the **PBDB-TF:BTBOL4F** binary blend film excited at λ = 760 nm is shown in our previous report, and the ultrafast hole transfer is observed within 300

fs.[28] Addition of **$PC_{71}BM$** accelerates the hole transfer in the **PBDB-TF:BTBOL4F:$PC_{71}BM$** ternary blends, as the bleach deepens with $k_1 \sim 2 \times 10^{12}$ s^{-1} and 3×10^{12} s^{-1} (Figures S35-S36) rate constants for the ternary **8:6:2** and **8:3:5** blends, respectively. Again, because of the similar donor-acceptor energetics, this observation indicates a similar alteration of the interfacial contact between the polymer and acceptor regions of the films. Interestingly, the TA result is also confirmed by the film morphology data (Figures S22, S23, and S24). From the GIWAXS analysis of **PBDB-TF:BTBOL4F:$PC_{71}BM$** blends, the additional fullerene results in an increased volume fraction of ordered polymer, acceptor domains, and an overall higher crystallinity of the **8:6:2** ternary blend.

Charge recombination in the photoactive layers was further evaluated quantitatively by light intensity (I) dependence measurements (Figure S8).[56] All the plots of V_{OC} versus ln(I) show linear relations, and the ideality factor n can be calculated from the extracted slope nk_BT/e, where k_B is the Boltzmann constant, T is the temperature, and e is the elementary charge.[57, 58] **PBDB-TF:$PC_{71}BM$**, **PBDB-TF:ITIC-Th**, and **8:6:2** ternary blend films yield a slope of 1.85 k_BT/e, 1.13 k_BT/e, and 1.54 k_BT/e, respectively. This indicates that BR loss is dominant in the **PBDB-TF:ITIC-Th** blend, and adding **$PC_{71}BM$** results in both significant contribution from Shockley-Read-Hall (SRH) recombination and BR (smaller component). The recombination between stationary charges in deep traps and oppositely charged mobile carriers was first proposed by Shockley and Read.[59, 60] In the same experiment, J_{SC} follows a function as, $J_{SC} \sim I^{\alpha}$, where α is an exponential factor related to device BR loss -- the steeper slope implies a lower BR.[58] Plots of **PBDB-TF:$PC_{71}BM$**, **PBDB-TF:ITIC-Th**, and ternary **8:6:2** blends show α values of 0.904, 0.919, 0.923, respectively, in good agreement with the photovoltaic device performance. The results suggest that BR is suppressed in the optimal ternary **8:6:2** BHJ blend.

From the results of the TA spectroscopy, light intensity dependence measurements, and structural data over multiple length scales, we infer that the addition of small amounts of **$PC_{71}BM$** retains the crystallinity of **ITIC-Th** in the ternary blend, enabling electron delocalization from **ITIC-Th** domains to **$PC_{71}BM$** domains, thereby suppressing the BR of the **PBDB-TF:ITIC-Th** FCs, and simultaneously increasing **PBDB-TF:$PC_{71}BM$** CT pairs as new charge separation and extraction pathways. This results in enhanced FC photo-generation and thus J_{SC} and PCE. However, excess **$PC_{71}BM$** in turn increases absorptive losses and parasitic decay pathways (Figure S33), such as through the **$PC_{71}BM$** triplet state,[16] thereby decreasing FC generation and ultimately, PCE. These conclusions are further supported by DFT computations based on the single crystal structures as discussed below.

Theory and Simulations

A single **ITIC-Th** acceptor molecule and a short oligomer (three repeat units) of the **PBDB-TF** donor polymer were optimized *in vacuo* and the frontier molecular orbitals (FMOs) were visualized (Figure S39); the highest occupied molecular orbital (HOMO) and lowest unoccupied molecular orbital (LUMO) energy levels correlate reasonably well with the CV data (Figure 1), and their HOMO-LUMO gaps are in good agreement, 2.10 eV and 1.88 eV, respectively. Both the HOMO and the LUMO of **ITIC-Th** extend fully across the breadth of the π-structure, but those of **PBDB-TF** just touch the terminal units of the oligomer, suggesting that combining the three units is reasonable for modelling the FMO wavefunctions. The vertical ionization energy and vertical electron affinity of **ITIC-Th** are 6.39 eV and 2.74 eV, respectively, which are ideal for NFA to pair with a donor such as **PBDB-TF**. Furthermore, the **ITIC-Th** internal hole and electron reorganization energies are 180 meV and 170 meV, respectively, in good agreement with similar NFA structures.[50]

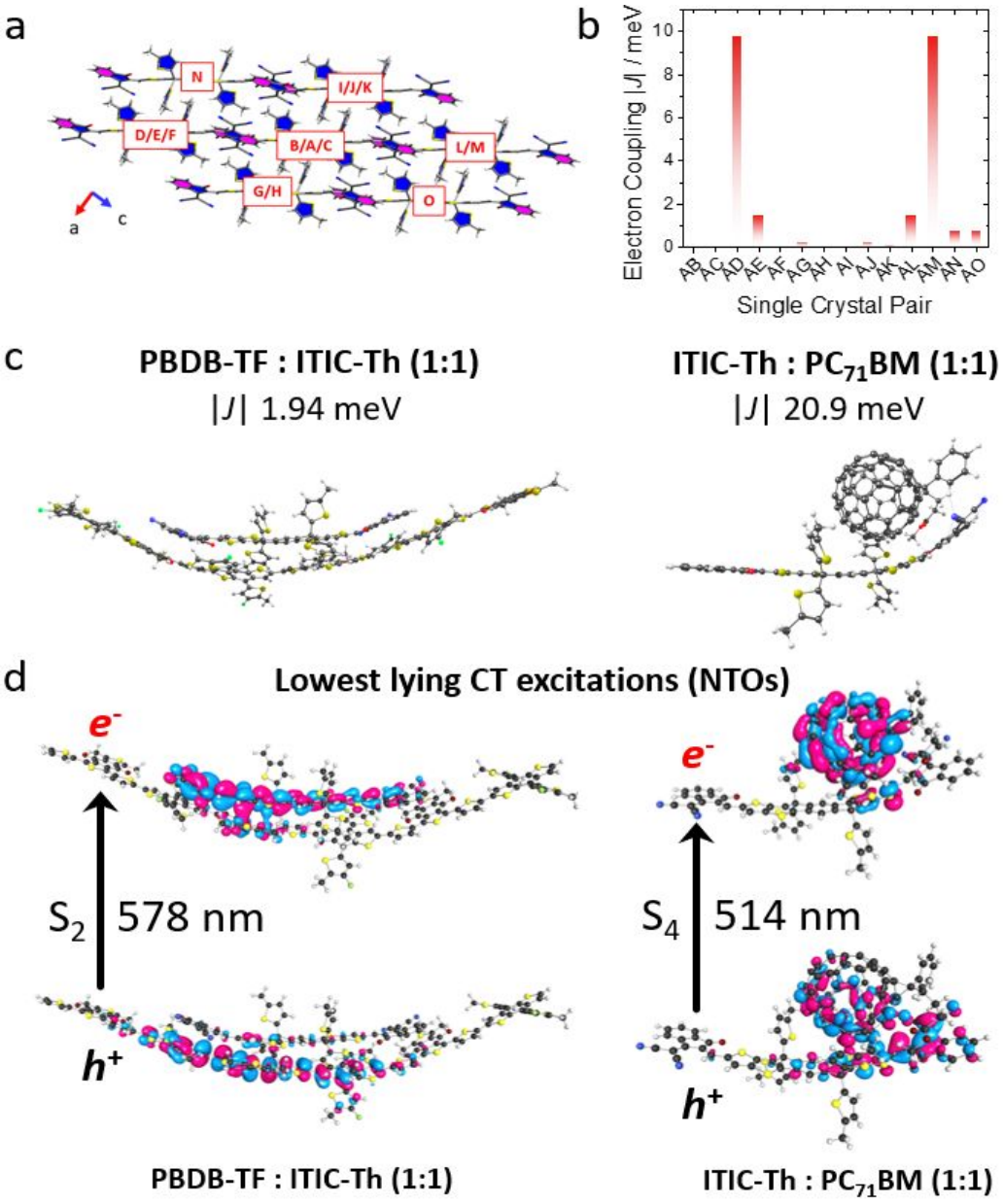

Figure 7. **Theory and simulations of intermolecular interactions in the indicated donor-acceptor units. a**, **ITIC-Th** single crystal with the alkyl chains truncated to methyl groups labelled with alphabetic identifiers; **b,** Electronic coupling between dimer pairs of A and surrounding near-neighbors (B-O). **c,** Electronic coupling between 1:1 optimized dimers of selected structures. (Left) **PBDB-TF:ITIC-Th**, (right) **ITIC-Th:PC$_{71}$BM**; **d,** Excited state NTOs of the hole (h^+) and electron (e^-) for CT excited states of (left) **PBDB-TF:ITIC-Th** and (right) **ITIC-Th:PC$_{71}$BM** optimized dimers. The CT-like transitions for h^+ and e^- in the available excited states are shown for the S_2 and S_4 NTOs, respectively. The NTO densities are plotted with a +/- 0.02 isosurface.

The **ITIC-Th** single crystal data were next analyzed by DFT (see Methods and the SI), to analyze electronic coupling between pairs of molecules, to probe pathways for charge transfer and the extent of intermolecular interaction in the solid phase. The process involves the identification of a molecule with the maximum number of near-neighbors around it in the single crystal (high symmetry point, labeled as A). Every neighbor is also labelled and the coupling between each pair consisting of structure A and a neighbor, such as AB, AC... *etc.*, is computed (Figure 7a). The couplings $|J|$, presented in Figure 7b, show that the highest electronic coupling occurs in two pairs, AD ($|J|$ = 9.78 meV) and AM ($|J|$ = 9.80 meV), with the latter being the maximum coupling $|J_{max}|$.

This is not far from the basic **ITIC** structure[29] ($|J|$ = 16.14 meV), but is more than half that of **Y6** ($|J|$ = 37.9 meV).[41] The electronic couplings were investigated further, by optimizing dimers of **ITIC-Th** and **PBDB-TF** (Figure S40) and **$PC_{71}BM$**. We find that the **PDBD-TF:ITIC-Th** optimized dimer has an electronic coupling of just 1.94 meV (Figure 7c, left), while the **ITIC-Th:$PC_{71}BM$** dimer is 20.9 meV (Figure 7c, right). This might seem surprising at first, as one might expect stronger coupling between the donor polymer **PBDB-TF** and the **ITIC-Th** NFA, yet in our previous studies[50, 52] we found that the coupling is greatest between acceptor-acceptor moieties, reflecting the nature of the charge transport through these channels. Here then, the larger coupling correlates with the experimental observations that the ternary blend exhibits higher solar cell performance and SCLC electron mobility than binary blends.

The FMOs of these dimer structures were next computed and are illustrated in Figure S44. In both systems, the LUMO is localized on the **ITIC-Th** structure, while the HOMO is localized on the **PBDB-TF** and the **$PC_{71}BM$** moieties. This supports the transient absorption data and photophysical model (Figure 6) that following excitation of **ITIC-Th** and hole transfer to the **PBDB-TF**, the remaining electron from the charged-separated state will preferentially reside on

the **ITIC-Th**, followed by delocalization to **$PC_{71}BM$**. The excited-state electronic structure of the three molecules used in the device were therefore examined using time-dependent density functional theory (TD-DFT, see Methods). Using the transition density matrix, we calculated the natural transition orbitals (NTOs) for both **PBDB-TF** and **ITIC-Th**. The excited states of **$PC_{71}BM$** have been calculated previously using numerous levels of theory and DFT functionals.[61-63] The NTOs for **PBDB-TF** and **ITIC-Th** are shown in Figure S45, with the **PBDB-TF** oligomer shown for $n = 3$ monomers. The NTOs of the hole and electron are illustrated separately for each molecule. Both **PBDB-TF** and **ITIC-Th** have $\pi \rightarrow \pi^*$ character for the first excitation S_1 (Figure S45), although the **PBDB-TF** has some CT character. In contrast, **ITIC-Th** has a pure $\pi \rightarrow \pi^*$ transition as seen by the resemblance to the HOMO and LUMO in Figure S39. The transition density matrix was further examined to visualize the size of the hole and electron (see SI for details). The electron (hole) size for **ITIC-Th** is 7.6 Å (7.0 Å), while for **PBDB-TF** the size is about 50 % larger at 11.0 Å (11.1 Å). Analyzing the separation between the electron and hole we find the distance is marginally larger for **PBDB-TF** as well with a separation of 6.7 Å vs 6.5 Å.

The natural transition orbitals (NTOs) of the **PBDB-TF:ITIC-Th** and **ITIC-Th:$PC_{71}BM$** heterodimers were next computed to understand the charge separation capacity at the interfaces. Using the geometries obtained from the optimized dimers in Figure 7, it is found that the heterodimers have many low-lying dark CT character excitations along with a weak oscillator strength S_1 excitation (see SI). We represent the two lower lying CT character excited states for each heterodimer (S_2 and S_4) in Figure 7d using the NTOs of the transition density. Compared to the FMOs of the dimer structures (Figures S42-S44), the NTO excitations have strong CT character but with minimal oscillator strength. Importantly, the energies are within the exciton energy range of **PBDB-TF** and **ITIC-Th** (Figure S45). Note also that the CAM-B3LYP functional used in the

TDDFT calculations is known to introduce a significant blue shift (≈0.3 eV) leading to a mismatch of singlet state energies versus the fsTA bleach at 720 nm. This low-lying CT character for excited states matches up well with the fsTA spectra (FC-1 to FC-2, Figure 6a) that show near isoenergetic FC states as the carriers delocalize across the interface. Overall, the theory and simulation results support the 1D charge transport via the malonitrile EG stacking in **ITIC-Th** molecules, high μ_e, and the photophysics model in ternary blend films.

Conclusions and Outlook

The results of this study reveal a general relationship between BHJ film morphology and charge-dynamics performance in the binary and ternary BHJ blends of organic semiconductors. We have shown here that the optimal incorporation of **$PC_{71}BM$** into the **PBDB-TF:ITIC-Th** binary system retains the original π-face-on molecular orientations relative to the device electrodes, **ITIC-Th** crystallinity, BHJ domain dimensions, and decreases the BHJ film upper surface **ITIC-Th** content. It does not significantly affect the overall morphology of the **PBDB-TF:ITIC-Th** binary blend. While these morphology changes increase hole and electron mobilities simultaneously, they also facilitate electron delocalization from **ITIC-Th** to **$PC_{71}BM$** domains, reduce FC bimolecular recombination, increase another FC extraction pathway through the **PBDB-TF:$PC_{71}BM$** pair, therefore resulting in significantly enhanced inverted solar cell J_{SC} and FF. Interestingly, we observe that as the **$PC_{71}BM$** content is increased, excessive incorporation of **$PC_{71}BM$** into **PBDB-TF:ITIC-Th** binary system alters **PBDB-TF** orientation to π-edge-on relative to the electrode, diminishes **ITIC-Th** rich regions, decreases **ITIC-Th** crystallinity, while increasing large scale **$PC_{71}BM$**-rich aggregations and BHJ top surface **$PC_{71}BM$** content. These morphology changes promote parasitic photon loss pathways through the **$PC_{71}BM$**-rich domains, thereby compromising J_{SC}, FF, and PCE significantly. By increasing the **$PC_{71}BM$** content and decreasing the NFA content,

the ternary J_{SC} and FF decrease first, then increase, and finally decrease with mostly unchanged V_{OC}s, leading to synchronous PCE fluctuation, and the optimal polymer:NFA:fullerene blending weight ratio for high PCE is found to be 8:6:2. This correlation with device performance indicates that a high **ITIC-Th** crystallinity and presence of large **ITIC-Th**-rich regions is key to maximizing PSC performance. Single crystal X-ray diffraction of **ITIC-Th** reveals two novel types of sidechain-supported π-π stackings and provides an example of long-distance (> 4 Å) coupling between EGs. Based on the experimentally determined **ITIC-Th** crystal and **$PC_{71}BM$** crystal structures, DFT calculations find that the electronic coupling between neighbors of **ITIC-Th** molecules (≈10 meV) is half as large as the coupling within an **ITIC-Th:$PC_{71}BM$** dimer (20.9 meV). The LUMO density also preferentially resides on the **ITIC-Th** unit, rather than on the **PBDB-TF** or **$PC_{71}BM$** units, supporting the hypothesis that the electron generated via charge separation resides on the **ITIC-Th** structure before delocalization and subsequent 1D charge transport to **$PC_{71}BM$**. Regarding the generality of this model, we find that J_{SC}, FF, and PCE enhancement is also observed in the **Y6**-skeleton-based NFA **BTBOL4F** BHJ blends and affords significantly enhanced PSC performance, achieving high PCEs ≈ 17 %. Overall, these types of structure-performance correlations and mechanistic understandings should benefit the soft matter solar research community and will stimulate attempts to achieve higher organic solar cell PCEs > 20 % in the future.

Methods

Experimental details can be found in SI Appendix.

Solar cell and single carrier diode measurements. Solar cell fabrication, current density-voltage (J-V), external quantum efficiency (EQE), light intensity dependence measurements, and data processing were conducted following the standard procedure in this Laboratory as described in a

previous report.[64] Single carrier diode device fabrication, measurements, and data processing were performed following the standard procedure in this laboratory as described in a previous report.[64]

Atomic force microscopy characterization. AFM tapping mode measurements were conducted on a SPID Bruker ICON, and blend films were prepared using the same conditions as for PSC device fabrication.

Transmission electron microscopy analysis. TEM specimens were prepared on PSS-covered glass substrates, using identical conditions as the actual PSC devices (see details in the solar cell fabrication section). The PSS layer was cast onto glass substrates (VWR) from mass fraction of 18 % poly(4-styrenesulfonic acid) water solution (Sigma-Aldrich 561223-500G) after filtering through a Nylon filter (0.45 μm), spin-coated at 5000 rpm (524 rad/s) 30 s, ACL = 6000, and annealed at 120 °C for 10 min in air. The substrates were transferred to deionized water and the floated organic films were transferred onto the copper TEM grid with a lacey carbon coating (Ted Pella, Inc.). TEM images were obtained on a Hitachi HT7700 microscope in the bright field mode at an acceleration of 120 kV.

LAADF-STEM characterization. LAADF-STEM images of each specimen were collected using an FEI Titan 80-300 STEM (FEI Company, Hillsboro, Oregon) equipped with a double-hexapole spherical aberration corrector (CEOS GmbH, Heidelberg, Germany) and an annular dark-field detector (Model 3000, E. A. Fischione Instruments, Export, Pennsylvania). A small (3 mrad) probe-forming aperture was used and the post-specimen optics were configured such that the ADF detector inner and outer angles were 17 mrad and 95 mrad, respectively. A low spot number was used to produce an electron probe containing a current of approximately 45 pA when using the small probe-forming aperture. A 2D fast Fourier transform (FFT) was calculated from each image (Scipy, fftpack).

Grazing incidence 2θ X-ray diffraction. GIXRD measurements were conducted on a Rigaku Smartlab with monochromated CuKα radiation (λ = 1.541 Å). Omega was set as 0.2, while 2θ was scanned from 2° to 30°. Data analysis was in OriginPro 9 software, and diffraction peaks were fitted with Bragg's equation $n \times \lambda = 2d \times \sin\theta$ to obtain lamellar (d_{100}) and π-π (d_{010}) stacking distances, respectively. All the films were prepared on ZnO/Si substrates.

GIWAXS characterization. GIWAXS was measured at the Stanford Synchrotron Radiation Light source (SSRL) beamline 11-3 and at the 11-BM Complex Materials Scattering (CMS) beamline of the National Synchrotron Light Source II (NSLS-II). At SSRL the samples were placed in a He-filled chamber, and an X-ray energy of 12.7 keV and sample to detector distance of 340 mm, at an incident angle of 0.12°. The images were recorded with a 2D X-ray detector (MX225, Rayonix LLC) with a pixel size of 73 μm (3072 × 3072 pixels). GIWAXS measurements at CMS were performed with a beam energy of 13.5 keV. The 2D scattering patterns were collected at an X-ray incidence angle of 0.14° with a Pilatus 1M detector with a pixel size of 172 μm and placed about 250 mm from the sample. Data were analyzed using the Nika package[65] for Igor Pro software (WaveMetrics, Inc.). In this work, the polar angle (χ) is defined as the angle of the observed diffraction from the normal to the substrate. Thus, χ = 0° is perpendicular to the substrate and χ = 90° is parallel to the substrate. The out-of-plane sector is considered at 0 to 20°, and the in-plane sector is 70 to 90°. GIWAXS pole figures were constructed from the 2D data after correcting for **ITIC-Th** mass fractions, sample thickness, missing wedge, as well as detector solid angle effects. Sector-averaged 1D profiles were obtained from 15° cake sectors in the in-plane and out-of-plane directions. Coherence lengths were obtained by multi-peak fitting of the profiles using multiple Gaussian peaks on a polynomial background. At first the neat samples were fitted

following the above procedure. Peak positions and widths were obtained from neat films were then used as starting values to fit the data from the blends.

RSoXS measurements. This resonant scattering technique exploits the optical contrast between the polymer and **ITIC-Th** molecules near the carbon 1s absorption edge. The scattering contrast for a 2-component system is directly proportional to $\Delta\delta_{12}^2 + \Delta\beta_{12}^2$, where the complex refractive index $n = 1 - \delta + i\beta$. The real part of the complex refractive index $(1 - \delta)$ is related to dispersion and the imaginary part (β) is related to absorption. The scattering arises from composition correlations weighted by scattering contrast and respective volume fractions of these correlations. The scattering profile is the Fourier transform of the scattering density in a sample with the dominant peak representing the domain spacing or the median size scale.

RSoXS measurements were performed in transmission geometry at the ALS beamline 11.0.1.2.[66] BHJ active layers were cast on 2 cm × 2 cm Si/PEDOT:PSS substrate. Blends were prepared using the same conditions as PSC devices. RSoXS samples of the BHJ films were prepared by a wet floatation method. The films were scored with a scalpel and then introduced to a bath of deionized water. The bottom-most sacrificial organic layer (PSS) was dissolved leaving the BHJ active layer floating on the water surface. The floating films were then transferred onto a 100 nm Si_3N_4 window (Norcada) for RSoXS measurements. The 2D data were collected using an in-vacuum [base pressure ≈10^{-9} kPa (10^{-8} mBar)] CCD detector (PIMTE, Princeton Instruments, 2048 × 2048 pixels). 1D scattering profiles were obtained from the 2D scattering patterns using a custom Nika.[65] 11 analysis package and normalized for the instantaneous X-ray flux.

NEXAFS characterization. X-ray absorption measurements in partial electron yield (PEY) mode were performed at the Soft X-ray Spectroscopy beamline at the Australian Synchrotron. Linearly polarized photons (P ≈ 1) from an undulator X-ray source with spectral resolution of E/ΔE ≤ 10,000

were focused to a beam size of ≈100 μm × 100 μm onto samples in an ultrahigh vacuum chamber. PEY spectra were measured using a channeltron detector. NEXAFS samples were prepared on 2 cm × 2 cm Si substrate under identical conditions as those for the optimized PSC devices and analyzed using the QANT[67] analysis package. The recorded spectra were normalized to the incident photon flux using a gold mesh and further normalized by setting the pre-edge signal in the range (270 to 275) eV to 0 and normalizing the post-edge signal in the range (335 to 340) eV to 1. Surface composition was determined by fitting a linear combination of neat reference spectra to blend spectra acquired at the magic incidence angle of ≈ 54.7°.

UV-vis absorption spectroscopy. UV-vis spectra of the samples were obtained on a Varian Cary 100 UV-vis spectrophotometer. Films were spincast onto clean glass substrates (VWR).

TA spectroscopy. Femtosecond transient absorption spectroscopy (fsTA) experiments were performed using a regeneratively-amplified Ti:sapphire laser system (Tsunami Oscillator / Spitfire Pro amplifier, Spectra-Physics) as previously described.[68] Briefly, the UV-vis continuum probe (λ ~ 400−800 nm) was generated by focusing the λ = 827 nm fundamental (100 fs, 2 μJ) into a 2 mm sapphire plate. The NIR continuum probe (λ ~ 850 nm to 1600 nm) was generated by focusing the λ = 827 nm fundamental (100 fs, 3 μJ) into a 10 mm proprietary crystal (Ultrafast Systems, LLC). The samples were irradiated at λ_{ex} = 720 nm with ≈110 fs, 0.12 μJ pulses of 1 mm spot size with randomized polarization (DPU-25-A, Thorlabs, Inc) to suppress observation of polarizartion-dependent dynamics. The λ_{ex} = 720 nm excitation pulse was generated with a home-built optical parametric amplifier.[69] Transient spectra were acquired with 3 s averaging at each time delay point. The fsTA data were corrected for group delay dispersion, or chirp, and scattered light prior to the analysis using Surface Xplorer (Ultrafast Systems, LLC).

Electronic structure analysis. Structural optimizations of the acceptors **ITIC-Th** and **$PC_{71}BM$** were computed using DFT in ORCA[70] The B3LYP[71] functional was used in conjunction with a dispersion correction using Grimme's third generation dispersion with Becke Johnson damping (D3BJ). We used a triple zeta valence (TZV), s and p larger polarization set (PP) Karlsruhe type basis set (def2-TZVPP) as developed by Weigend and Ahlrich.[72] This level of theory for the DFT calculations was used in the calculation of vacuum energies, frontier molecular orbitals, vertical ionization energies, vertical electron affinities, and internal reorganization energies for **ITIC-Th** and **$PC_{71}BM$**. Details of molecular orbital visualization are presented in the SI.

The structure of the **PBDB-TF** polymer was simplified to three repeat units and optimized using DFT. This provided satisfactory orbital energies in correlation with values obtained from cyclic voltammetry. The dimers were obtained from taking the optimized individual structures (**PBDB-TF**, **ITIC-Th**, **$PC_{71}BM$**) and added their coordinates together by hand at centrally placed and co-facial to each other with an assumed π-π separation of ≈3.4 Å. These dimer coordinates were then optimized without any constraint. The electronic couplings for the **ITIC-Th** single crystal and the dimers were computed as described in ref.[50] For further details of the dimer construction and structural optimizations see the SI.

Excited state calculations on the **PBDB-TF** and **ITIC-Th** monomers, and **$PC_{71}BM$:ITIC-Th** dimer were performed with the Q-Chem package[73] using TD-DFT. The TD-DFT functional CAM-B3LYP[74] was used to account for the long-range hole-electron interaction. Details are provided in the SI (Section 14).

References

1. Y. Wei, Z. Chen, G. Lu, N. Yu, C. Li, J. Gao, X. Gu, X. Hao, G. Lu, Z. Tang, J. Zhang, Z. Wei, X. Zhang and H. Huang, *Adv. Mater.*, 2022, **n/a**, 2204718.
2. K. Yoshikawa, H. Kawasaki, W. Yoshida, T. Irie, K. Konishi, K. Nakano, T. Uto, D. Adachi, M. Kanematsu, H. Uzu and K. Yamamoto, *Nat. Energy*, 2017, **2**, 17032.
3. P.-J. Ribeyron, *Nat. Energy*, 2017, **2**, 17067.

4. Y. Liu, B. Dong, A. Hagfeldt, J. Luo and M. Graetzel, *SmartMat*, 2021, **2**, 33-37.
5. T. J. Aldrich, W. Zhu, S. Mukherjee, L. J. Richter, E. Gann, D. M. DeLongchamp, A. Facchetti, F. S. Melkonyan and T. J. Marks, *Chem. Mater.*, 2019, **31**, 4313-4321.
6. Y. Cui, Y. Xu, H. Yao, P. Bi, L. Hong, J. Zhang, Y. Zu, T. Zhang, J. Qin, J. Ren, Z. Chen, C. He, X. Hao, Z. Wei and J. Hou, *Adv. Mater.*, 2021, **33**, e2102420.
7. C. Li, J. Zhou, J. Song, J. Xu, H. Zhang, X. Zhang, J. Guo, L. Zhu, D. Wei, G. Han, J. Min, Y. Zhang, Z. Xie, Y. Yi, H. Yan, F. Gao, F. Liu and Y. Sun, *Nat. Energy*, 2021, **6**, 605-613.
8. L. Zhu, M. Zhang, J. Xu, C. Li, J. Yan, G. Zhou, W. Zhong, T. Hao, J. Song, X. Xue, Z. Zhou, R. Zeng, H. Zhu, C.-C. Chen, R. C. I. MacKenzie, Y. Zou, J. Nelson, Y. Zhang, Y. Sun and F. Liu, *Nat. Mater.*, 2022, **21**, 656-663.
9. L. Lu, T. Zheng, Q. Wu, A. M. Schneider, D. Zhao and L. Yu, *Chem. Rev.*, 2015, **115**, 12666-12731.
10. J. Chen, Y. Chen, L.-W. Feng, C. Gu, G. Li, N. Su, G. Wang, S. M. Swick, W. Huang, X. Guo, A. Facchetti and T. J. Marks, *EnergyChem*, 2020, **2**, 100042.
11. G. Chai, Y. Chang, J. Zhang, X. Xu, L. Yu, X. Zou, X. Li, Y. Chen, S. Luo, B. Liu, F. Bai, Z. Luo, H. Yu, J. Liang, T. Liu, K. S. Wong, H. Zhou, Q. Peng and H. Yan, *Energy Environ. Sci.*, 2021, DOI: 10.1039/d0ee03506h.
12. W. Gao, F. Qi, Z. Peng, F. R. Lin, K. Jiang, C. Zhong, W. Kaminsky, Z. Guan, C. S. Lee, T. J. Marks, H. Ade and A. K. Jen, *Adv. Mater.*, 2022, **n/a**, e2202089.
13. J. Yuan, Y. Q. Zhang, L. Y. Zhou, G. C. Zhang, H. L. Yip, T. K. Lau, X. H. Lu, C. Zhu, H. J. Peng, P. A. Johnson, M. Leclerc, Y. Cao, J. Ulanski, Y. F. Li and Y. P. Zou, *Joule*, 2019, **3**, 1140-1151.
14. G. Li, L.-W. Feng, S. Mukherjee, L. O. Jones, R. M. Jacobberger, W. Huang, R. M. Young, R. M. Pankow, W. Zhu, N. Lu, K. L. Kohlstedt, V. K. Sangwan, M. R. Wasielewski, M. C. Hersam, G. C. Schatz, D. M. DeLongchamp, A. Facchetti and T. J. Marks, *Energy Environ. Sci.*, 2022, **15**, 645-659.
15. W. R. Mateker and M. D. McGehee, *Adv. Mater.*, 2017, **29**, 1603940.
16. A. Rao, P. C. Y. Chow, S. Gelinas, C. W. Schlenker, C.-Z. Li, H.-L. Yip, A. K. Y. Jen, D. S. Ginger and R. H. Friend, *Nature*, 2013, **500**, 435-439.
17. A. J. Gillett, A. Privitera, R. Dilmurat, A. Karki, D. Qian, A. Pershin, G. Londi, W. K. Myers, J. Lee, J. Yuan, S.-J. Ko, M. K. Riede, F. Gao, G. C. Bazan, A. Rao, T.-Q. Nguyen, D. Beljonne and R. H. Friend, *Nature*, 2021, **597**, 666-671.
18. R. Noriega, J. Rivnay, K. Vandewal, F. P. V. Koch, N. Stingelin, P. Smith, M. F. Toney and A. Salleo, *Nat. Mater.*, 2013, **12**, 1038-1044.
19. L. Ye, H. Hu, M. Ghasemi, T. Wang, B. A. Collins, J. H. Kim, K. Jiang, J. H. Carpenter, H. Li, Z. Li, T. McAfee, J. Zhao, X. Chen, J. L. Y. Lai, T. Ma, J. L. Bredas, H. Yan and H. Ade, *Nat. Mater.*, 2018, **17**, 253-260.
20. G. Han and Y. Yi, *Acc. Chem. Res.*, 2022, **55**, 869-877.
21. L. Zhu, M. Zhang, W. Zhong, S. Leng, G. Zhou, Y. Zou, X. Su, H. Ding, P. Gu, F. Liu and Y. Zhang, *Energy Environ. Sci.*, 2021, **14**, 4341-4357.
22. L. Chang, M. Sheng, L. Duan and A. Uddin, *Org. Electron.*, 2021, **90**, 106063.
23. M. Zhang, X. Guo, W. Ma, H. Ade and J. Hou, *Adv. Mater.*, 2015, **27**, 4655-4660.
24. T. J. Aldrich, S. M. Swick, F. S. Melkonyan and T. J. Marks, *Chem. Mater.*, 2017, **29**, 10294-10298.

25. S. Li, L. Ye, W. Zhao, X. Liu, J. Zhu, H. Ade and J. Hou, *Adv. Mater.*, 2017, DOI: 10.1002/adma.201704051, 1704051-n/a.
26. Y. Lin, F. Zhao, Q. He, L. Huo, Y. Wu, T. C. Parker, W. Ma, Y. Sun, C. Wang, D. Zhu, A. J. Heeger, S. R. Marder and X. Zhan, *J. Am. Chem. Soc.*, 2016, **138**, 4955-4961.
27. Y. Lin, J. Wang, Z. G. Zhang, H. Bai, Y. Li, D. Zhu and X. Zhan, *Adv. Mater.*, 2015, **27**, 1170-1174.
28. G. Li, X. Zhang, L. O. Jones, J. M. Alzola, S. Mukherjee, L. W. Feng, W. Zhu, C. L. Stern, W. Huang, J. Yu, V. K. Sangwan, D. M. DeLongchamp, K. L. Kohlstedt, M. R. Wasielewski, M. C. Hersam, G. C. Schatz, A. Facchetti and T. J. Marks, *J. Am. Chem. Soc.*, 2021, **143**, 6123-6139.
29. S. M. Swick, W. Zhu, M. Matta, T. J. Aldrich, A. Harbuzaru, J. T. Lopez Navarrete, R. Ponce Ortiz, K. L. Kohlstedt, G. C. Schatz, A. Facchetti, F. S. Melkonyan and T. J. Marks, *Proc Natl Acad Sci U S A*, 2018, **115**, E8341-E8348.
30. Y. Chen, P. Ye, Z. G. Zhu, X. Wang, L. Yang, X. Xu, X. Wu, T. Dong, H. Zhang, J. Hou, F. Liu and H. Huang, *Adv. Mater.*, 2017, **29**, 1603154-n/a.
31. S. Halaby, M. W. Martynowycz, Z. Zhu, S. Tretiak, A. Zhugayevych, T. Gonen and M. Seifrid, *Chem. Mater.*, 2021, **33**, 966-977.
32. X. Guo, N. Zhou, S. J. Lou, J. Smith, D. B. Tice, J. W. Hennek, R. P. Ortiz, J. T. L. Navarrete, S. Li, J. Strzalka, L. X. Chen, R. P. H. Chang, A. Facchetti and T. J. Marks, *Nat. Photon.*, 2013, **7**, 825-833.
33. H. Yao, L. Ye, J. Hou, B. Jang, G. Han, Y. Cui, G. M. Su, C. Wang, B. Gao, R. Yu, H. Zhang, Y. Yi, H. Y. Woo, H. Ade and J. Hou, *Adv. Mater.*, 2017, **29**, 1700254-n/a.
34. R. Yu, S. Zhang, H. Yao, B. Guo, S. Li, H. Zhang, M. Zhang and J. Hou, *Adv. Mater.*, 2017, DOI: 10.1002/adma.201700437, 1700437-n/a.
35. W. Zhao, S. Li, S. Zhang, X. Liu and J. Hou, *Adv. Mater.*, 2017, **29**, 1604059-n/a.
36. P. N. Murgatroyd, *Journal of Physics D: Applied Physics*, 1970, **3**, 151-156.
37. G. G. Malliaras, J. R. Salem, P. J. Brock and C. Scott, *Phys. Rev. B*, 1998, **58**, 13411-13414.
38. V. D. Mihailetchi, J. K. J. van Duren, P. W. M. Blom, J. C. Hummelen, R. A. J. Janssen, J. M. Kroon, M. T. Rispens, W. J. H. Verhees and M. M. Wienk, *Adv. Funct. Mater.*, 2003, **13**, 43-46.
39. Y. He and Y. Li, *Phys. Chem. Chem. Phys.*, 2011, **13**, 1970-1983.
40. W. Zhao, S. Li, H. Yao, S. Zhang, Y. Zhang, B. Yang and J. Hou, *J. Am. Chem. Soc.*, 2017, **139**, 7148-7151.
41. W. Zhu, A. P. Spencer, S. Mukherjee, J. M. Alzola, V. K. Sangwan, S. H. Amsterdam, S. M. Swick, L. O. Jones, M. C. Heiber, A. A. Herzing, G. Li, C. L. Stern, D. M. DeLongchamp, K. L. Kohlstedt, M. C. Hersam, G. C. Schatz, M. R. Wasielewski, L. X. Chen, A. Facchetti and T. J. Marks, *J. Am. Chem. Soc.*, 2020, **142**, 14532-14547.
42. N. D. Eastham, A. S. Dudnik, T. J. Aldrich, E. F. Manley, T. J. Fauvell, P. E. Hartnett, M. R. Wasielewski, L. X. Chen, F. S. Melkonyan, A. Facchetti, R. P. H. Chang and T. J. Marks, *Chem. Mater.*, 2017, **29**, 4432-4444.
43. Y. Huang, E. J. Kramer, A. J. Heeger and G. C. Bazan, *Chem. Rev.*, 2014, **114**, 7006-7043.
44. S. Gélinas, A. Rao, A. Kumar, S. L. Smith, A. W. Chin, J. Clark, T. S. van der Poll, G. C. Bazan and R. H. Friend, *Science*, 2014, **343**, 512-516.
45. G. Wang, S. M. Swick, M. Matta, S. Mukherjee, J. W. Strzalka, J. L. Logsdon, S. Fabiano, W. Huang, T. J. Aldrich, T. Yang, A. Timalsina, N. Powers-Riggs, J. M. Alzola, R. M.

Young, D. M. DeLongchamp, M. R. Wasielewski, K. L. Kohlstedt, G. C. Schatz, F. S. Melkonyan, A. Facchetti and T. J. Marks, *J. Am. Chem. Soc.*, 2019, **141**, 13410-13420.
46. T. J. Aldrich, M. Matta, W. Zhu, S. M. Swick, C. L. Stern, G. C. Schatz, A. Facchetti, F. S. Melkonyan and T. J. Marks, *J. Am. Chem. Soc.*, 2019, **141**, 3274-3287.
47. X. J. Li, I. Angunawela, Y. Chang, J. D. Zhou, H. Huang, L. Zhong, A. Liebman-Pelaez, C. H. Zhu, L. Meng, Z. Q. Xie, H. Ade, H. Yan and Y. F. Li, *Energy Environ. Sci.*, 2020, **13**, 5028-5038.
48. G. Zhang, X. K. Chen, J. Xiao, P. C. Y. Chow, M. Ren, G. Kupgan, X. Jiao, C. C. S. Chan, X. Du, R. Xia, Z. Chen, J. Yuan, Y. Zhang, S. Zhang, Y. Liu, Y. Zou, H. Yan, K. S. Wong, V. Coropceanu, N. Li, C. J. Brabec, J. L. Bredas, H. L. Yip and Y. Cao, *Nat. Commun.*, 2020, **11**, 3943.
49. H. Chen, H. Lai, Z. Chen, Y. Zhu, H. Wang, L. Han, Y. Zhang and F. He, *Angew. Chem. Int. Ed.*, 2021, **60**, 3238-3246.
50. S. M. Swick, J. M. Alzola, V. K. Sangwan, S. H. Amsterdam, W. Zhu, L. O. Jones, N. Powers-Riggs, A. Facchetti, K. L. Kohlstedt, G. C. Schatz, M. C. Hersam, M. R. Wasielewski and T. J. Marks, *Adv. Energy Mater.*, 2020, **10**, 2000635.
51. H. Huang, L. Yang, A. Facchetti and T. J. Marks, *Chem. Rev.*, 2017, **117**, 10291-10318.
52. S. M. Swick, T. Gebraad, L. Jones, B. Fu, T. J. Aldrich, K. L. Kohlstedt, G. C. Schatz, A. Facchetti and T. J. Marks, *Chemphyschem*, 2019, **20**, 2608-2626.
53. H. Huang, Z. Chen, R. P. Ortiz, C. Newman, H. Usta, S. Lou, J. Youn, Y.-Y. Noh, K.-J. Baeg, L. X. Chen, A. Facchetti and T. Marks, *J. Am. Chem. Soc.*, 2012, **134**, 10966-10973.
54. H. Yan, Z. Chen, Y. Zheng, C. Newman, J. R. Quinn, F. Dotz, M. Kastler and A. Facchetti, *Nature*, 2009, **457**, 679-686.
55. X. Zhan, A. Facchetti, S. Barlow, T. J. Marks, M. A. Ratner, M. R. Wasielewski and S. R. Marder, *Adv. Mater.*, 2011, **23**, 268-284.
56. G. Lakhwani, A. Rao and R. H. Friend, *Annu. Rev. Phys. Chem.*, 2014, **65**, 557-581.
57. A. K. K. Kyaw, D. H. Wang, V. Gupta, W. L. Leong, L. Ke, G. C. Bazan and A. J. Heeger, *Acs Nano*, 2013, **7**, 4569-4577.
58. S. R. Cowan, A. Roy and A. J. Heeger, *Phys. Rev. B*, 2010, **82**, 245207.
59. R. N. Hall, *Phys. Rev.*, 1952, **87**, 387-387.
60. W. Shockley and W. T. Read, *Phys. Rev.*, 1952, **87**, 835-842.
61. T. Kastinen, D. A. da Silva Filho, L. Paunonen, M. Linares, L. A. Ribeiro Junior, O. Cramariuc and T. I. Hukka, *Phys. Chem. Chem. Phys.*, 2019, **21**, 25606-25625.
62. Y. Li, T. Pullerits, M. Zhao and M. Sun, *J. Phys. Chem. C*, 2011, **115**, 21865-21873.
63. G. Grancini, D. Polli, D. Fazzi, J. Cabanillas-Gonzalez, G. Cerullo and G. Lanzani, *J. Phys. Chem. Lett.*, 2011, **2**, 1099-1105.
64. W. G. Zhu, J. M. Alzola, T. J. Aldrich, K. L. Kohlstedt, D. Zheng, P. E. Hartnett, N. Eastham, W. Huang, G. Wang, R. M. Young, G. C. Schatz, M. R. Wasielewski, A. Facchetti, F. S. Melkonyan and T. J. Marks, *ACS Energy Lett.*, 2019, **4**, 2695-2702.
65. J. Ilavsky, *J. Appl. Crystallogr.*, 2012, **45**, 324-328.
66. E. Gann, A. T. Young, B. A. Collins, H. Yan, J. Nasiatka, H. A. Padmore, H. Ade, A. Hexemer and C. Wang, *Rev. Sci. Instrum.*, 2012, **83**, 045110.
67. E. Gann, C. R. McNeill, A. Tadich, B. C. C. Cowie and L. Thomsen, *J. Synchrotron. Radiat*, 2016, **23**, 374-380.
68. R. M. Young, S. M. Dyar, J. C. Barnes, M. Juríček, J. F. Stoddart, D. T. Co and M. R. Wasielewski, *J. Phys. Chem. A*, 2013, **117**, 12438-12448.

69. *Opt. Lett.*, 1995, **20**, 1394-1396.
70. F. Neese, *WIREs Computational Molecular Science*, 2012, **2**, 73-78.
71. A. D. Becke, *J. Chem. Phys.*, 1993, **98**, 5648-5652.
72. F. Weigend and R. Ahlrichs, *Phys. Chem. Chem. Phys.*, 2005, **7**, 3297-3305.
73. Y. Shao, Z. Gan, E. Epifanovsky, A. T. B. Gilbert, M. Wormit, J. Kussmann, A. W. Lange, A. Behn, J. Deng, X. Feng, D. Ghosh, M. Goldey, P. R. Horn, L. D. Jacobson, I. Kaliman, R. Z. Khaliullin, T. Kuś, A. Landau, J. Liu, E. I. Proynov, Y. M. Rhee, R. M. Richard, M. A. Rohrdanz, R. P. Steele, E. J. Sundstrom, H. L. Woodcock, P. M. Zimmerman, D. Zuev, B. Albrecht, E. Alguire, B. Austin, G. J. O. Beran, Y. A. Bernard, E. Berquist, K. Brandhorst, K. B. Bravaya, S. T. Brown, D. Casanova, C.-M. Chang, Y. Chen, S. H. Chien, K. D. Closser, D. L. Crittenden, M. Diedenhofen, R. A. DiStasio, H. Do, A. D. Dutoi, R. G. Edgar, S. Fatehi, L. Fusti-Molnar, A. Ghysels, A. Golubeva-Zadorozhnaya, J. Gomes, M. W. D. Hanson-Heine, P. H. P. Harbach, A. W. Hauser, E. G. Hohenstein, Z. C. Holden, T.-C. Jagau, H. Ji, B. Kaduk, K. Khistyaev, J. Kim, J. Kim, R. A. King, P. Klunzinger, D. Kosenkov, T. Kowalczyk, C. M. Krauter, K. U. Lao, A. D. Laurent, K. V. Lawler, S. V. Levchenko, C. Y. Lin, F. Liu, E. Livshits, R. C. Lochan, A. Luenser, P. Manohar, S. F. Manzer, S.-P. Mao, N. Mardirossian, A. V. Marenich, S. A. Maurer, N. J. Mayhall, E. Neuscamman, C. M. Oana, R. Olivares-Amaya, D. P. O'Neill, J. A. Parkhill, T. M. Perrine, R. Peverati, A. Prociuk, D. R. Rehn, E. Rosta, N. J. Russ, S. M. Sharada, S. Sharma, D. W. Small, A. Sodt, T. Stein, D. Stück, Y.-C. Su, A. J. W. Thom, T. Tsuchimochi, V. Vanovschi, L. Vogt, O. Vydrov, T. Wang, M. A. Watson, J. Wenzel, A. White, C. F. Williams, J. Yang, S. Yeganeh, S. R. Yost, Z.-Q. You, I. Y. Zhang, X. Zhang, Y. Zhao, B. R. Brooks, G. K. L. Chan, D. M. Chipman, C. J. Cramer, W. A. Goddard, M. S. Gordon, W. J. Hehre, A. Klamt, H. F. Schaefer, M. W. Schmidt, C. D. Sherrill, D. G. Truhlar, A. Warshel, X. Xu, A. Aspuru-Guzik, R. Baer, A. T. Bell, N. A. Besley, J.-D. Chai, A. Dreuw, B. D. Dunietz, T. R. Furlani, S. R. Gwaltney, C.-P. Hsu, Y. Jung, J. Kong, D. S. Lambrecht, W. Liang, C. Ochsenfeld, V. A. Rassolov, L. V. Slipchenko, J. E. Subotnik, T. Van Voorhis, J. M. Herbert, A. I. Krylov, P. M. W. Gill and M. Head-Gordon, *Mol. Phys.*, 2015, **113**, 184-215.
74. T. Yanai, D. P. Tew and N. C. Handy, *Chem. Phys. Lett.*, 2004, **393**, 51-57.

Acknowledgements

This research was supported in part by the Center for Light Energy Activated Redox Processes (LEAP), an Energy Frontier Research Center funded by the U.S. Department of Energy, Office of Science, Office of Basic Energy Sciences under Award Number DE-SC0001059 (W.Z. single crystal growth, devices, microscopy, GIXRD; L.O.J., K.L.K., G.C.S. theory; J.L.L., N.E.P.-R., R.M.Y., M.R.W. fs/ns TA; T.J.M., A.F., W.Z. project discussions). This work was also supported by the US Department of Commerce, National Institute of Standards and Technology as part of the Center for Hierarchical Materials Design Award 70NANB10H005 (F.S.M. materials synthesis and characterization); the U.S. Office of Naval Research Contract #N00014-20-1-2116 (G.L.,

materials synthesis, T.J.M., A.F., project direction); and the Qatar National Research Foundation grant NPRP12S-0304-190227/02-484761 (G.L. material synthesis, solar cell fabrication). This work made use of the EPIC, Keck-II, and/or SPID facilities of Northwestern's NUANCE Center, which received support from the Soft and Hybrid Nanotechnology Experimental (SHyNE) Resource (NSF ECCS-1542205). Use of the Advanced Photon Source, an Office of Science User Facility operated for the U.S. Department of Energy Office of Science by Argonne National Laboratory Part of this research was undertaken on the Soft X-ray Spectroscopy beamline at the Australian Synchrotron, part of ANSTO. Use of the Stanford Synchrotron Radiation Lightsource, SLAC National Accelerator Laboratory, is supported by the U.S. Department of Energy (DOE), Office of Science, Office of Basic Energy Sciences under Contract No. DE-AC02-76SF00515. Use of the 11-BM (CMS) beamline of the National Synchrotron Light Source II, operated by Brookhaven National Laboratory is supported by the DOE Office of Science under Contract No. DE-SC0012704. RSoXS data were acquired at the Advanced Light Source, which was supported by the Director, Office of Science, Office of Basic Energy Sciences, of the DOE under Contract DE-AC02-05CH11231. Beamline support at beamline 11.0.1.2 was provided by A. L. D. Kilcoyne and C. Wang. W. Zhu thanks the Open Foundation of State Key Laboratory of Electronic Thin Films and Integrated Devices (KFJJ202001, Unconventional Organic Nonlinear Optical Hybrid Materials and Devices) for partial financial support. The authors thank Prof. B. Savoie of Purdue University for valuable discussions. Certain commercial equipment, instruments, materials or software are identified in this paper in order to specify the experimental procedure adequately. Such identification is not intended to imply recommendation or endorsement by NIST, nor is it intended to imply that the materials or equipment identified are necessarily the best available for the purpose. W. Zhu sincerely thanks S. Li for the support in completing this manuscript.

Author contributions

W.Z. fabricated and measured a portion of the solar cells, and characterized the films using AFM, TEM, GIXRD, UV-vis absorption spectra, and charge carrier mobility (SCLC); G.L. synthesized **BTBOL4F**, fabricated and measured part of solar cells; W.Z. grew the single crystals of **ITIC-Th**, C.S. determined the structure, G.L. analysis the single crystal molecular packings; W.Z. and G.L. prepared the films, R.J.K. and L.F. performed two-dimensional GIWAXS, S.M., E.G. performed RSoXS experiments, D.M.D., E.G., S.M. performed NEXAFS experiments, S.M. analyzed the data; A.H. performed STEM measurements; W.Z. prepared the films, J.L., N.P., R.Y.

performed fsTA experiments, J.L., N.P., R.Y., W.Z. analyzed and discussed the data; L.J. and K.K. conducted simulations and provided discussions; W.Z., K.K., G.S., D.D., M.W., F.M., A.F., T.J.M. coordinated the project; All the authors discussed the results, wrote, and approved the final manuscript and supplementary information.

Additional information

Supplementary information is available online. Correspondence and requests for materials should be addressed to W.Z., K.L.K., G.C.S., D.M.D., M.R.W, F.S.M., A.F., T.J.M.

Competing interests

The authors declare no competing financial interests.